Fall 1-31-2009

Experiment and modeling : ignition of aluminum particles with a CO2 laser

Salil Mohan
New Jersey Institute of Technology

ABSTRACT

EXPERIMENT AND MODELING: IGNITION OF ALUMINUM PARTICLES WITH A CO_2 LASER

by
Salil Mohan

Aluminum is a promising ingredient for high energy density compositions used in propulsion systems, explosives, and pyrotechnics. Aluminum powder fuel additives enable one to achieve higher combustion enthalpies and reaction temperatures. Therefore, to develop aluminum based novel and customized high density energetic materials, understanding of ignition and combustion kinetics of aluminum powders is required. In most practical systems, metal ignition and combustion occur in environments with rapidly changing temperatures and gas compositions. The kinetics of exothermic reactions in related energetic materials is commonly characterized by thermal analysis, where the heating rates are very low, on the order of 1 – 50 K/min. The extrapolation of the identified kinetics to the high heating rates is difficult and requires direct experimental verification. This difficulty led to development of new experimental approaches to directly characterize ignition kinetics for the heating rates in the range of 10^3 – 10^4 K/s. However, the practically interesting heating rates of 10^6 K/s range have not been achieved.

This work is directed at development of an experimental technique and respective heat transfer model for studying ignition of aluminum and other micron-sized metallic particles at heating rates varied around 10^6 K/s. The experimental setup uses a focused CO_2 laser as a heating source and a plate capacitor aerosolizer to feed the aluminum particles into the laser beam. The setup allows using different environment for particle

aerosolization. The velocities of particles in the jet are in the range of 0.1 –0 3 m/s. For each selected jet velocity, the laser power is increased until the particles are observed to ignite. The ignition is detected optically using a digital camera and a photomultiplier. The ignition thresholds for spherical aluminum powder were measured at three different particle jet velocities, in air environment. A single particle heat transfer model was developed to describe the experiments. Experiments with different jet velocities in air environment were performed to validate the model.

The interaction of the laser beam with particles is particle size dependent and a narrow range of particle sizes (around 3.4 μm) is heated most effectively. Therefore, the heat transfer model needs to be analyzed only for the particles with this specific size, which greatly simplifies the interpretation of experiments. Describing heating of a micron sized metal particle involves the transition regime heat transfer. A modified Fuchs model was used to describe the heat transfer in this study.

In addition to dry air environment, the experimental technique was also used with other oxidizing environments, including O_2, H_2O, CO_2 and mixtures thereof. It was observed that particle size capable of maintaining a vapor phase flame is a function of the environment. Arrhenius model kinetics parameters for Al ignition in O_2, CO_2 and H_2O environments were determined.

EXPERIMENT AND MODELING: IGNITION OF ALUMINUM PARTICLES WITH A CO_2 LASER

by
Salil Mohan

A Dissertation
Submitted to the Faculty of
New Jersey Institute of Technology
in Partial Fulfillment of the Requirements for the Degree of
Doctor of Philosophy in Mechanical Engineering

Department of Mechanical Engineering

January 2009

APPROVAL PAGE

EXPERIMENT AND MODELING: IGNITION OF ALUMINUM PARTICLES WITH A CO_2 LASER

Salil Mohan

12/4/2008

Dr. Edward L. Dreizin, Dissertation Advisor — Date
Professor, Otto H. York Department of Chemical, Biological and Pharmaceutical Engineering, NJIT

12/4/2008

Dr. Boris Khusid, Committee Member — Date
Professor, Otto H. York Department of Chemical, Biological and Pharmaceutical Engineering, NJIT

12/04/08

Dr. Kwabena A Narh, Committee Member — Date
Professor, Department of Mechanical Engineering, NJIT

12/04/08

Dr. Suhithi M. Peiris, Committee Member — Date
Basic Research Sciences Team Lead, Defense Threat Reduction Agency (DTRA)

12/04/08

Dr. Mirko Schoenitz, Committee Member — Date
Research Professor, Otto H. York Department of Chemical, Biological and Pharmaceutical Engineering, NJIT

BIOGRAPHICAL SKETCH

Author: Salil Mohan

Degree: Doctor of Philosophy

Date: January 2009

Undergraduate and Graduate Education:

- Doctor of Philosophy in Mechanical Engineering,
  New Jersey Institute of Technology, Newark, NJ, 2009
- Master of Science in Mechanical Engineering,
  New Jersey Institute of Technology, Newark, NJ, 2003
- Bachelor of Technology in Mechanical Engineering,
  G. B. Pant Univ. of Agri. & Tech., Pantnager, India 1987

Major: Mechanical Engineering

Presentations and Publications:

Mohan S., Trunov, M. A. and Dreizin, E. L. (2008). Heating and Ignition of Metallic Particles by a CO2 Laser. Journal of Propulsion and Power, 24 (2), 199-205.

Mohan S., Trunov, M. A. and Dreizin, E. L. (2008). Heating and Ignition of Metal Particles in the Transition Heat Transfer Regime. Journal of Heat Transfer, 130 (10), 104505 – 104509.

Mohan S. Trunov M. A. Dreizin, E.L., (2007). Heating and Ignition of Metallic Particles by a CO_2 Laser. 45th AIAA Aerospace Sciences Meeting Proceedings.

Mohan, S. Shoshin, Y.L. Dreizin, E.L. (2006). Ignition of Aerosolized Reactive Particles at High Heating Rates. Materials Research Society Symposium Proceedings, (Multifunctional Energetic Materials), 896, 165-170.

Mohan, S, Trunov, M.A. and Dreizin, E.L. (2003). Characterization of Al Powder Ignition. Technical Fall Meeting, Eastern State Section of Combustion Institute, Pennsylvania State University, PA, USA

To my wife, Kavita

ACKNOWLEDGMENT

I would like to express my deepest appreciation to Dr. Edward L Dreizin, who not only served as my research supervisor, providing valuable and countless resources, insight, and intuition, but also constantly gave me support, encouragement, and reassurance. Special thanks are given to Dr.Suhithi Peiris, Dr. Boris Khusid, Dr. Mirko Schoenitz and Dr. Kwabena A Narh for actively participating in my committee.

Many thanks to Dr. Mikhaylo A. Trunov for his invaluable inputs towards my research work. I also wish to thank members of my research group for their support.

TABLE OF CONTENTS

TABLE OF CONTENTS
(Continued)

TABLE OF CONTENTS
(Continued)

Chapter **Page**

LIST OF TABLES

LIST OF FIGURES

LIST OF FIGURES
(Continued)

LIST OF FIGURES
(Continued)

LIST OF FIGURES
(Continued)

Figure **Page**

LIST OF FIGURES
(Continued)

Figure **Page**

CHAPTER 1

INTRODUCTION AND BACKGROUND

1.1 Problem Statement

Reactive metals and metalloids, e.g., Al, B, Mg, Zr, Ti, Li, etc., as well as their alloys are promising ingredients for high energy density compositions used in propulsion systems, explosives, and pyrotechnics. Metallic powder fuel additives enable one to achieve higher combustion enthalpies and reaction temperatures. In most practical systems, metal ignition and combustion occur in environments with rapidly changing temperatures and gas compositions.

On the other hand, most of the available quantitative characteristics describing ignition and combustion of metal particles were obtained from laboratory experiments in which the environment temperature and composition were carefully maintained. Thus, ignition of metallic particles has been often characterized by a specific ignition temperature, e.g., [1, 2] typically, corresponding to a specific experimental situation. Ignition is also commonly assumed to occur after a delay, which is estimated as the time required for preheating the particle up to its ignition temperature.

Classically, the ignition temperature is understood in terms of the Semenov thermal theory as the minimum environment temperature which leads to self-sustaining combustion of an inserted particle [3, 4]. This definition has been successfully used for applications where the heating rates are characteristically low, e.g., dealing with fire safety and ignition of solid fuels in large furnaces [5, 6]. However, it becomes inadequate for applications in which the particles are heated rapidly, when the particle's temperature can exceed the classically defined ignition temperature before the self-

sustaining combustion is established. Furthermore, the whole concept of ignition temperature appears inadequate considering the nature of heterogeneous oxidation leading to ignition of most metals. For example, for aluminum, the thermally accelerated heterogeneous oxidation producing the heat necessary for a self-sustaining combustion also accelerates the growth of a protective oxide layer, which could prevent the combustion from occurring. This situation is typical for metal particle ignition in explosives, propellants and pyrotechnics.

Thus, to describe ignition for such applications, it is necessary to analyze specific transient heat transfer problems in which one or more of the exothermic processes leading to the particle ignition are considered. Such analyses require quantitative descriptions of these, typically thermally controlled, exothermic processes balanced by the conventional heat transfer terms of convection and radiation. The kinetics of exothermic reactions in related energetic materials is commonly characterized by thermal analysis, where the heating rates are very low, on the order of 1 – 50 K/min. The extrapolation of the identified kinetics to the high heating rates is difficult and requires direct experimental verification. This difficulty led to development of new experimental approaches to directly characterize ignition kinetics for the heating rates in the range of $10^3 - 10^4$ K/s [7, 8]. However, the practically interesting heating rates of 10^6 K/s have not been achieved. Also, there is a critical difficulty in the interpretation of all the experimental data dealing with ignition of metal powders, which is caused by the presence of particles of different sizes. The heating rates are different for particles of different sizes, and so must be the rates of the thermally controlled processes leading to ignition. Therefore, interpretation of the experimental data obtained with regular, poly-

dispersed metal powders is difficult while experiments with highly mono-dispersed particles are impractical.

This work presents a new experimental technique and the corresponding heat transfer model that enables one to quantify ignition kinetics for reactive particles heated at varied heating rates approaching to or exceeding 10^6 K/s. Aluminum, the most common reactive metal additive is used in this study. Many different approaches to describe aluminum ignition have been presented in literature. This chapter presents a brief experimental and theoretical background on aluminum ignition.

Efforts to characterize aluminum ignition till now have produced results that are inconsistent between them and often are contradictory. Figure 1.1 plots the published data on aluminum particle size and ignition temperature.

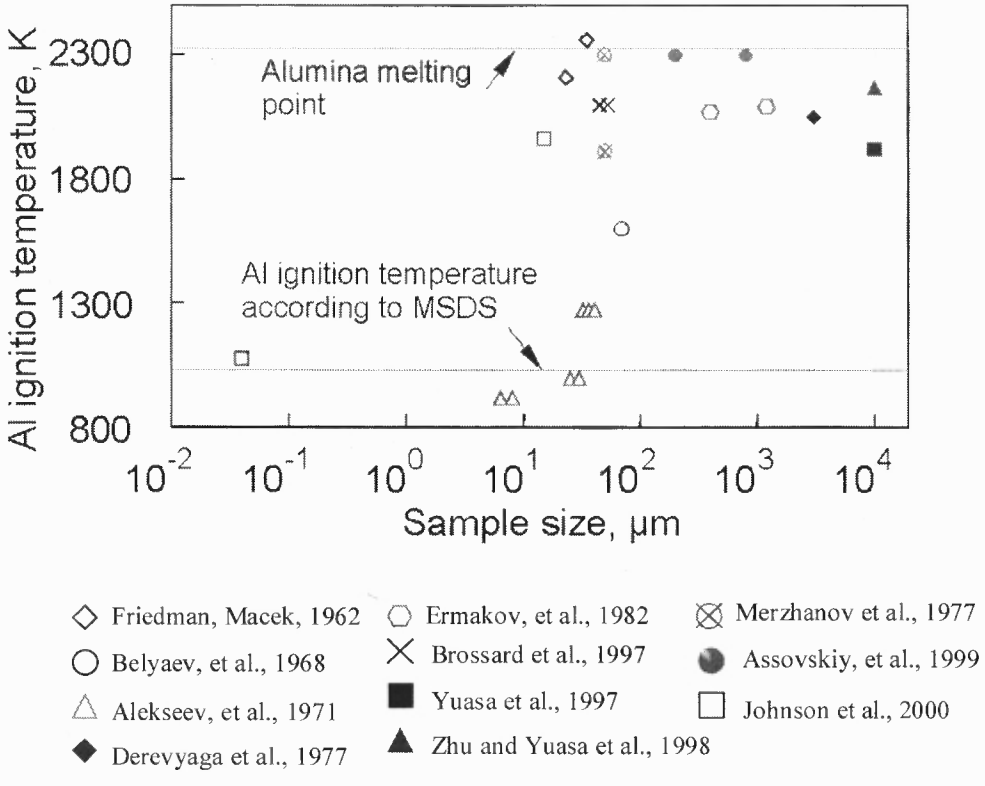

Figure 1.1 Summary of experimental results on aluminum ignition, [9-19].

Temperatures as low as 850 K and as high as 2300 K have been reported as aluminum ignition temperatures by different authors [9-19]. The reported ignition temperatures appear to correlate with the sample sizes [20]. The discrepancies between the points reported by different authors may be attributed to different experimental methods employed, which resulted in different conditions, such as heating rates and surrounding gas compositions. Also, different definitions of ignition moment used by different authors could have led to variations in the reported values of ignition temperatures.

1.2 Experimental Studies of Aluminum Ignition

Various experimental investigations focused on characterizing aluminum ignition have been reported in the literature [9-24]. Some characteristic examples of experimental techniques illustrating aluminum ignition in different heating regimes are described below.

1.2.1 Thermal Analysis

Thermogravimetry Analysis (TGA) and Differential Scanning Calorimetry (DSC) techniques are widely used in characterizing energetic materials [21, 22, 23] in a typical range of heating rates of 1 – 50 K/min. These rates are ideally suited for studying the heterogeneous oxidation kinetics of energetic materials but do not allow to directly characterize ignition and combustion of such materials. Recently published work [24-27] on aluminum oxidation using TGA technique indicates a stepwise process. Figure 1.2 from Ref. [24] illustrates a typical TGA trace showing the stepwise oxidation and associated weight increase. In the model proposed based on the TGA experiments [24],

the kinetic description for each observed oxidation step was proposed. The steps were prescribed to oxidation of different alumina polymorphs and to phase changes between such polymorphs. Assuming the ignition kinetics parameters and mechanisms derived from TGA experiments remain valid at higher heating rates, the ignition models can be developed used for practical applications.

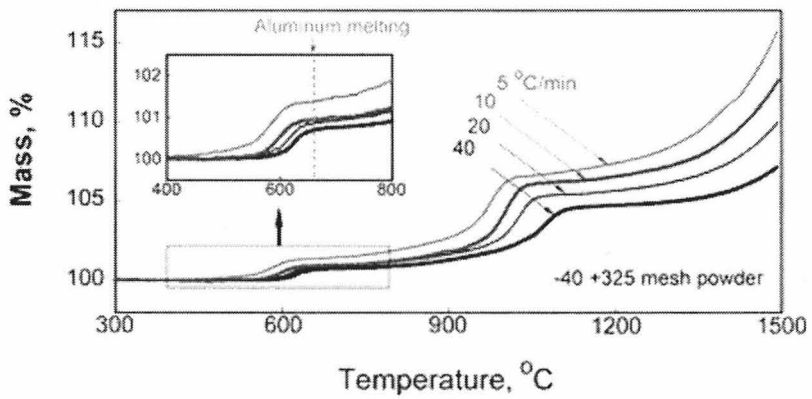

Figure 1.2 TGA technique showing mass increase of Al powder [24]. Stepwise weight increase indicates stepwise oxidation.

1.2.2 Wire Ignition Experiments

Ignition of pure Al is reported in literature [28-30] by heating Al wire electrically in a controlled gas environment. The reported heating rates with this technique are in the range of $10^2 - 10^3$ K/s. Ignition temperature for Al wire of 30 – 50 μm diameter wire in pure oxygen is reported to be in the range of 1900 – 2300 K [30]. The requirement to use a wire as the material sample is a limitation of this technique. A variant of this method was used recently to characterize energetic materials [7, 31]. Aluminum wire was replaced by a wire of a higher refractory alloy which was coated by a thin layer of a metal powder being investigated. Heating rates up to 10^5 K/s are reported. Figure 1.3 shows a schematic of the experimental setup used in this technique. Temperature is measured on

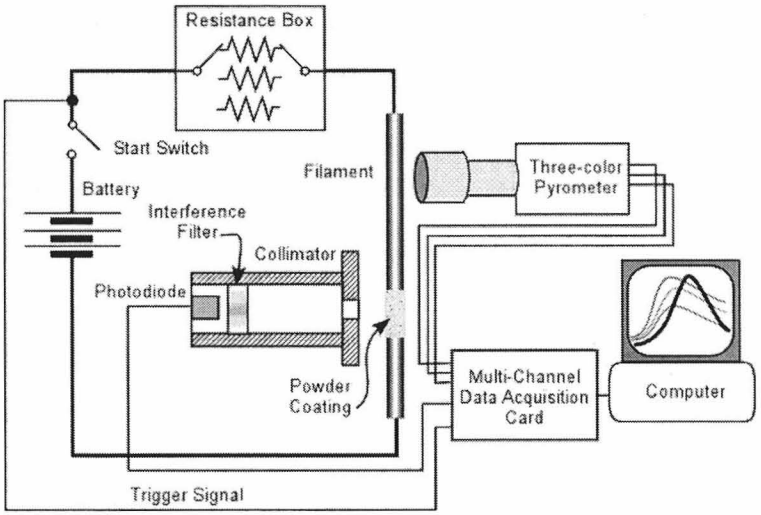

Figure 1.3 Schematic diagram of the experimental apparatus for powder ignition using an electrically heated filament [31].

the wire surface next to the coated powder and the powder ignition is detected optically. Ignition temperature measured is used to characterize the material. This method works well for materials with relatively low ignition temperatures. For aluminum, the metal wire was replaced by a carbon filament [31]. Ignition temperatures for 10 – 14 μm aluminum powder in air were reported to be in the range of 1750 – 1950 K [31], depending on the heating rates.

1.2.3 Shock Tube Experiments

Shock tube is a widely used and well studied tool for ignition of energetic materials in aerosol as well as gaseous state [32-36]. Experimental studies for ignition and combustion of aluminum powder in different environments were reported [35, 36]. This technique involves igniting the powder by a high temperature gas generated by a reflected shock wave at the end of a long steel tube. Upon passing the reflected shock, the

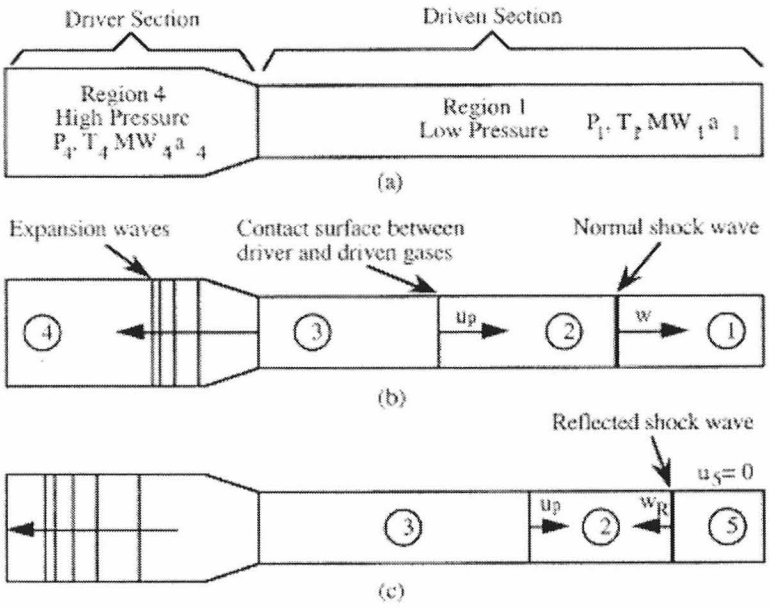

Figure 1.4 Shock-tube conditions: (a) before firing of the tube; (b) after firing, but before shock-wave reflection; and (c) after shock-wave reflection from end wall [35].

environment with temperature of the order of 2000 - 3500 K and pressures around 40 atm can be achieved [35]. Figure 1.4 from Ref. [35] illustrates the pressure regimes before, during and after the firing of the shock. The gas temperature rise can be achieved within half a millisecond and ignition of the particles can be diagnosed optically. Measured ignition delays and peak temperature of the particles were reported [35, 36]. However, assigning ignition temperature and ignition kinetics to a single particle in a shock tube experiments is difficult because the optical signal is captured from a particle cloud. In spite of this limitation very high heating rates of the order of 10^6 K/s are achievable.

1.3 Aluminum Ignition Models

A fixed ignition temperature is the most simple and straightforward model and it has produced satisfactory results for larger sized particle [24]. Particle ignition temperatures

are typically assumed in the vicinity of alumina melting point. In spite of some success with larger particle size this model does not explain the aluminum igniting over a wide range of temperatures, as shown in Figure 1.1. Two popular modeling approaches for ignition of aluminum particle are described below.

1.3.1 Oxide Shell Rapture Model

Aluminum particles are known to be coated with amorphous alumina layer [21]. The oxide shell rapture model takes into account the stresses in the alumina layer as a result of change in the volume of the aluminum metal core. This theory has been extensively discussed in literature [37-40]. It predicts ignition of the particle due to exposure of pure aluminum surface to the surrounding oxidizer through cracks in the protective amorphous alumina layer [39]. More recently, behavior of the alumina coating has been analyzed in the literature [41] and pressure build up in the core of the particle is predicted to be significant for smaller nano-aluminum particles. For all particle sizes, the pressure peaks near the melting point of Aluminum. Concepts of oxide shell spallation followed by pressure wave developing in the particles were discussed in Ref. [41]. This latter model is suggested to work at very high heating rates. Currently, no experimental support has been available for such models and the predictions are inconsistent with the reported thermal analysis experiments.

1.3.2 Polymorphic Phase Transformation Model

The alumina polymorphic phase transformation model [24-27] accounts for changes in the phase of alumina coating on the particle while the particle is heated. It describes the growth of oxide films along with transformation of different polymorphs and takes into

Table 1.1 Densities of Different Alumina Polymorphs Formed During Oxidation of Aluminum [24]

Polymorphs	*Density* (g/cm^3)
Amorphous -Al_2O_3	3 – 3.1
γ, δ, θ -Al_2O_3	3.6 – 3.67
α -Al_2O_3	3.99

account different activation energies for diffusion in different aluminum polymorphs and for phase change between those polymorphs. This model calculates the rate of oxidation that is limited by the rate of transport of oxygen or aluminum through the protective surface oxide layer. It has been reported that aluminum powders are coated with a 2.5-nm thick layer of amorphous alumina [42-45] which was the assumed initial oxide coating in the model. As the particle temperature increases, different polymorphs of Al_2O_3 become stable [24, 46] and the model considers kinetics of respective polymorphic phase transitions. The common route of phase transformations in alumina film grown on aluminum surface by thermal oxidation has been established in Ref [46] as: amorphous film $\rightarrow \gamma \rightarrow \delta \rightarrow \theta \rightarrow \alpha$ -Al_2O_3

In addition to different kinetics, the densities of these alumina polymorphs are also different from one another, as shown in Table 1.1 [24]. The transformations accompanied by significant increase in density of alumina, such as amorphous to γ-alumina and γ- to α alumina can also be accompanied by disruptions in continuity of the protective oxide. Thus, the oxidation rates and respective heat release rates are predicted to increase rapidly when such phase changes occur. Further details of the oxidation

model for aluminum particles are available in [27]. The validation of this model for aluminum ignition in air and its development for different oxidizing environments are the primary motivations of this research.

CHAPTER 2

EXPERIMENTAL SETUP AND DATA ANALYSIS

2.1 Introduction

The objective of this experimental effort is to study the heating and ignition of individual metal particles at heating rates in the range of 10^6 K/s. The technique should enable effective heating of particles only in a narrow range of sizes leading to the ignition of these narrowly selected particles.

The experimental setup uses a CO_2 laser for heating micron-sized particles in an oxidizing environment. Because the laser's wavelength (10.6 μm) and particle diameters are comparable, the efficiency of the particle heating by the laser beam is highly dependent on particle sizes [47]. At the threshold laser power, only particles with a very narrow range of sizes (around 3.4 μm) are heated efficiently and ignited. Thus, one needs to analyze the transient heat transfer only for the particles of this specific size, even though readily available poly-disperse powders are used in experiments. To ignite the particles, a laminar aerosol jet is fed into a focused CO_2 laser beam. The laser power is increased until the ignition is observed. A separate visible laser sheet is used to illuminate the particles in the jet for velocimetry. The particle speed could be readily controlled in the range of 0.1 - 3 m/s which enables experiments with varied heating rates. The experiment is conducted in an oxidizing environment, so that if the laser power exceeds a specific threshold, the heated particles of 3.4 μm diameter start igniting when they cross the laser beam.

A detailed heat transfer model is developed, taking into account heating of metal particles in the laser beam, thermally controlled heterogeneous exothermic reactions

leading to ignition, convection, and radiation terms. The model needs to consider only the specified above particle diameter, while experiments are conducted with a commercial poly-dispersed Al powder. The model includes one adjustable parameter that is the effective diameter of the focused laser beam. Specifically, it is the standard deviation for the Gaussian function describing the energy distribution across the laser beam. Note that the laser beam diameter is approximately determined from experiments as well, whereas an accurate measurement of the focused CO_2 laser beam diameter is difficult because of the thermal interaction of the beam and any target placed in its focal point. In addition, interference effects become substantial and contribute to the experimental error. Instead, an experimentally determined laser power ignition threshold obtained for spherical Al particles, for which the kinetics of exothermic reactions leading to ignition has been recently described [24-27] is used to determine the adjustable parameter (that is close to the measured value) and thus to calibrate the model.

2.2 Materials

Aluminum powder was used in the study: spherical Al, average particle size of 4.5 – 7 μm, 99% pure by Alfa Aesar.

2.3 Experimental Setup

The experimental setup is shown in Figure 2.1 and includes an aerosol jet generator, 125 W CO_2 laser (Synrad, Evolution 125) with a ZnSe convex lens (0.75″ aperture and 4″ focal length), and a modulated green laser (SUWTECH model DPGL-3000 by Photop Technologies, Inc) operated with a set of a semi-cylindrical and convex glass lenses to

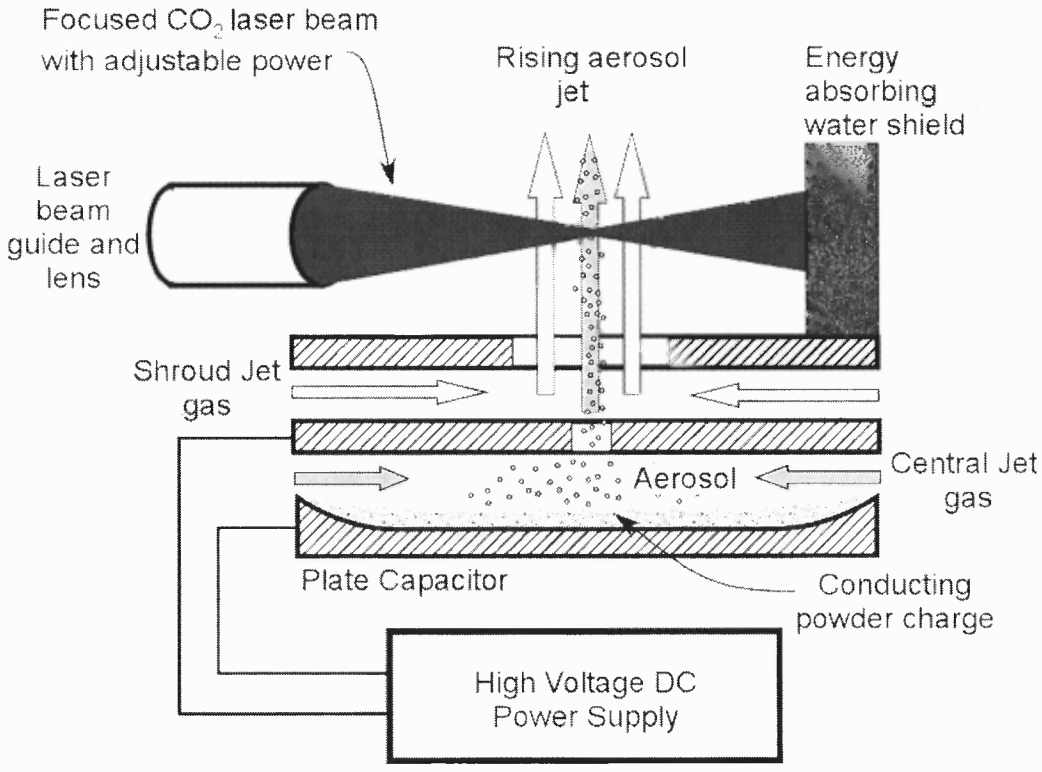

Figure 2.1 Schematic diagram of the experimental setup for studying particle ignition in a CO_2 laser beam.

produce a laser sheet for the jet visualization. Also, not shown in the Figure 2.1 but employed in the experiments were a digital camera (Panasonic GS-35), used to obtain particle streaks, and a photomultiplier tube (PMT) used to identify events of particle ignition. In addition, a power meter (Synrad, POWER WIZARD 250), was used to measure the laser beam energy and verify the accuracy of the pre-set laser power.

2.3.1 CO_2 Laser Operation

The experiment used the CO_2 laser to heat metal particles carried by oxidizing gas. The laser was operated by UC-2000 laser controller with a control gate voltage of 3 V for switching the laser. The typical beam output specifications given by the manufacturer are shown in Table 2.1.

Table 2.1 Manufacture's Output Parameter Specifications for CO_2 Laser

Parameters	*Model: Evolution 125*
Wave length	10.59 μm
Power Output (Continuous/Pulsed)	125/175 W
Power Stability	+ 5%
Mode Quality (at $1/e^2$)	TEM_{00}, 90% purity, $M^2 < 1.2$
Beam Waist size	4.4 mm
Beam Divergence (full angle)	3.2 mrad
Polarization	Linear/Vertical
Rise Time	< 150 μm
Modulation (optical response)	20 kHz

The laser power depends on both percentage output setting and modulation frequency, so a power meter with a resolution of $\pm$ 0.1 W was used to measure the output power. The laser power meter was placed in front of the CO_2 laser beam after the ZnSe focusing lens. It was placed for few seconds in front of the beam and an audible beep indicated the completion of the measuring cycle. The power was measured for each experimental run.

A ZnSe lens (Laser Mech, PLLPZ0063) with anti-reflection coatings and focal length of 4.0 in (for 10.6 μm wavelength) was used to focus the 4.4 mm CO_2 laser beam at the aerosol jet. A red laser diode (630 – 680 nm), collinear with the CO_2 laser beam, was used for alignment of the CO_2 laser beam. Because refractive index is a function of wavelength, the ZnSe lens has different focal length for the CO_2 laser beam and for the red laser used for alignment. In initial experiments in dry air, the particle jet was located at the focal point of the red laser (Chapter 4) while in following experiments (Chapter 5) the jet was positioned 4.0 in from the center of the ZnSe lens, in the nominal focal spot

for the CO_2 laser beam. The latter procedure gave a tighter focal spot, as discussed in Chapter 5.

A small tin vessel with thin walls filled with water was used for dumping the energy from the CO_2 beam after it crossed the particle jet. Liquid water is a very effective absorber of infrared radiation and has high specific heat, so that the water filled vessel absorbing the surplus of the CO_2 laser energy was not heated noticeably. Thus, the CO_2 beam target was an effective energy absorber, which did not emit any visible radiation that could interfere with the optical diagnostics used in the experiment.

In initial experiments in dry air, a CO_2 beam guide was used to deliver the beam to the ZnSe lens. The beam guide used two mirrors for two 90 ^{o} bends. Due to the heating of the mirror optics used in the beam guide, the CO_2 laser beam could occasionally misalign from the positioning red laser at higher laser power. The setup was later modified to directly deliver the CO_2 laser beam to the ZnSe lens without the use of any additional reflectors.

2.3.2 Electrostatic Powder Aerosolizer

The aerosol jet generator uses electrostatic aerosolization described elsewhere [48]. In this technique, a conductive (e.g., metal) powder is placed between the electrodes of a parallel plate capacitor. Figure 2.2 shows the schematic of the parallel plate electrostatic aerosolizer placed into a sealed, cylindrically shaped chamber (100 mm dia. and 60 mm height) with non-conducting side walls. The positive electrode has a plano-concave circular profile. Metallic powder is placed in the concave pit. The concave shape produces higher electric fields at the perimeter, preventing the powder from escaping from the capacitor.

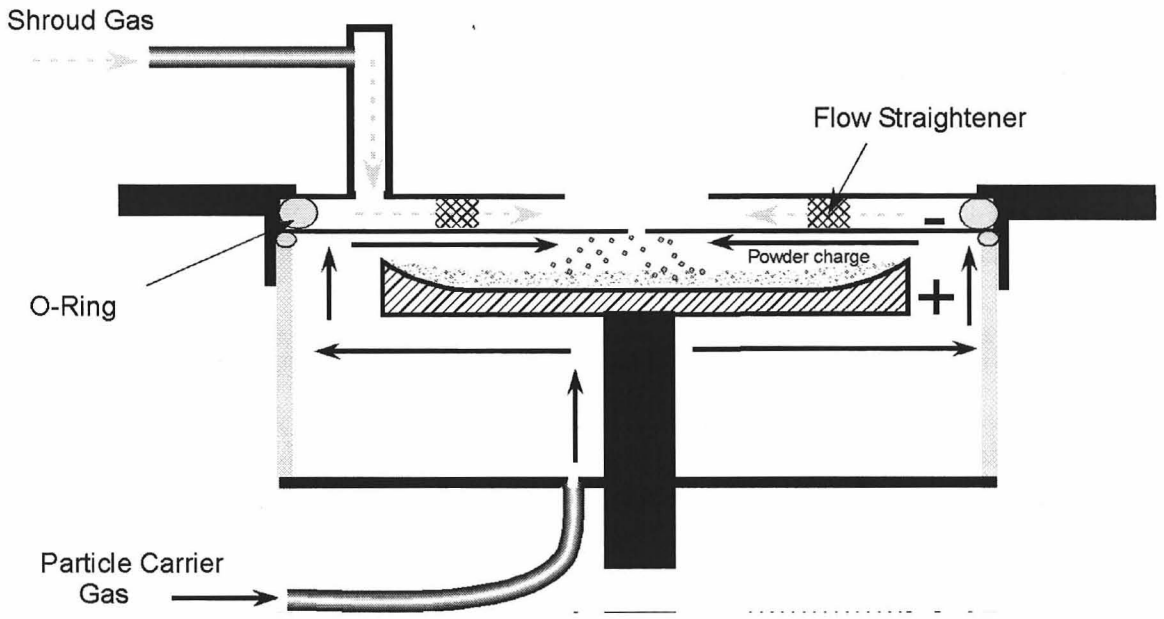

Figure 2.2 Schematic diagram of the parallel plate aerosolizer.

The top wall (cover) of the cylindrical chamber is made out of two parallel copper disks with the lower disk serving as the negative electrode. The two disks are separated by a 6.71 mm spacer with an o-ring seal. Both disks have circular openings (lower disk: 0.63 mm, upper disk 6.23 mm diameter) at the center for the escape of aerosol jet, as shown in Figure 2.2. A high DC voltage in the range of 1-15 kV is applied across the electrodes and the metallic particles acquire electric charge. The charged particles are repelled from the bottom electrode and attracted to the top electrode, at which they re-charge upon collision. The motion of the charging and re-charging particles continues so that an aerosol is produced in the space between the capacitor's electrodes. A small gas flow of the order of 100 ml/min, measured by a gas flow meter (M-200SCCM-D by Alicat Scientific Inc.), is fed into the chamber. The flow exits from the hole in the lower disk of the negative electrode carrying aerosolized particles and thus generating a fine jet of particles. Because of the multiple collisions of the charged particles with electrodes,

particle agglomerates are broken and the resulting jet contains single particles only, as was confirmed elsewhere [49]. A second gas flow of the order of 100 ml/min, measured by a gas flow meter (M-200SCCM-D by Alicat Scientific Inc.), is fed into the space between the two disks on the top of the chamber, creating a shroud flow around the fine jet coming out of the lower disk. The shroud flow was found to enhance the jet's stability [48] and helps separating the environment in the jet from the surrounding.

The DC voltage applied to the electrodes can be used to control the particle number density in the produced aerosol. In this project, the number density of the produced aerosol was restricted so that the number of particles fed into laser beam was of the order of 1000 per second. The air flow fed into the aerosolizer chamber was used to adjust the speed of the escaping aerosol jet. The speed could be readily controlled in the range of 0.1 - 3 m/s.

2.3.3 Particle Jet Velocimetry

The aerosol jet was illuminated by a vertical laser sheet created by a green laser (532 nm, SUWTECH model DPGL-3000 by Photop Technologies, Inc). A combination of a convex and semi-cylindrical lens was used to produce a green vertical laser sheet. To enable particle image velocimetry, the laser sheet was modulated at 300 - 3000 Hz, depending on the jet speed. Produced particle streaks were recorded using a digital camera (Panasonic GS-35) and the streak lengths were measured to determine the jet velocity. Figure 2.3 shows a particle in the jet in air at 0.57 m/s with the green laser modulated at 500 Hz. For each velocity measurement at least a total of 30 streaks were measured from different frames and the standard deviation was used as the error bar for the found average particle velocity.

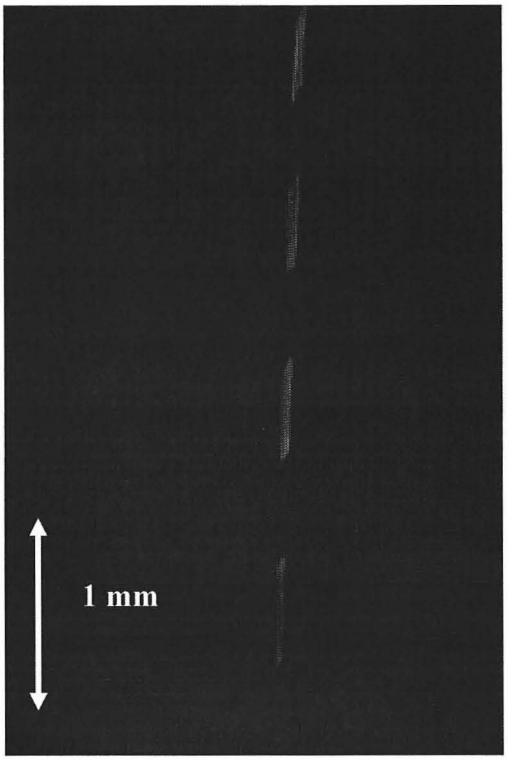

Figure 2.3 Particle streak recorded for a jet at 0.57 m/s illuminated by a green laser sheet modulated at 500 Hz.

2.3.4 Laser Spot Diameter

In a separate measurement, the effective diameter of the focused laser beam was evaluated. Because the laser energy is distributed across the beam according to a Gaussian profile [50], the laser beam diameter is poorly defined. However, experimentally this diameter was roughly assessed by firing the laser on a ceramic surface and measuring the diameter of the produced impression. For these measurements, the ceramic surface was placed in the focal spot of the red laser, so that the laser beam was somewhat defocused, as described in section 2.3.1.

Figure 2.4 shows magnified images of the impressions obtained at 12.5 W, 25 W and 62.5 W laser powers with exposure time of 90 ms, 15 ms and 3 ms respectively.

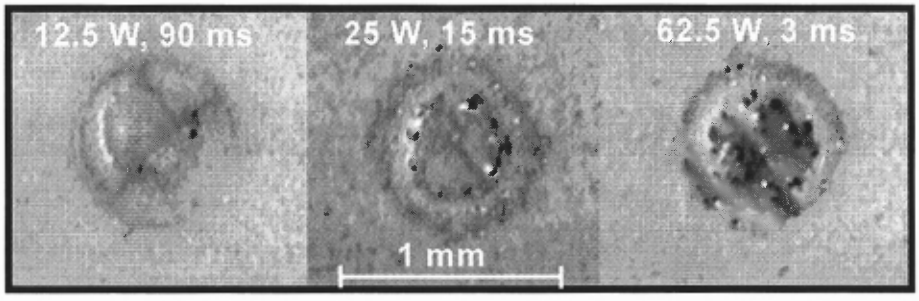

Figure 2.4 CO_2 laser beam impressions on a ceramic plate obtained at different laser power levels. The impressions are painted over with a dark marker to improve contrast. The laser powers and exposure times are shown for each impression.

Minimum exposure times required to obtain an impression were used for each laser power setting. The sizes of the external and internal circles observed on the obtained impressions did not change as a function of the laser power and could indicate the diameters of the zone of thermal influence and of the laser beam, respectively. The diameter of the inner circle was measured to be close to 330 μm. This size was considered as an initial approximation for the beam diameter. As described later, the width of the Gaussian distribution of the laser beam energy profile was used as an adjustable parameter in the developed heat transfer model. The measurement using the laser beam impressions served as a guide for the reasonable range, in which the adjustable parameter could vary.

2.3.5 Photo-multiplier Tube (PMT)

A 10.5 mm diameter PMT assembly by Hamamatsu, H3164-01, with detection range 300 to 650 nm was used to detect ignition and/or heating of the metal particles. The PMT was powered by a power supply C4710-01 by Hamamatsu. One of the four branches of a quadrifurcated optical cable (Spectra-Physics) was used to carry the signal to the PMT.

2.4 Experimental Procedure and Data Analysis

The CO_2 laser was focused about 1.5 cm above the jet nozzle using an auxiliary red laser aligned with the CO_2 laser beam and the ZnSe lens. Once a stable aerosol jet was established, the CO_2 laser was fired continuously for 8 seconds, at a preset power level. The visible radiation, generated by heating and/or ignition of particles, was monitored using a photomultiplier connected to a PC-based data acquisition system. The streaks of heated particles were also visualized by a digital camera operated with a shutter open for the entire duration of the laser firing, as shown in Figure 2.5. The experiment was repeated with gradually increased laser powers until ignition was clearly observed. The peaks recorded by the PMT were analyzed to determine the minimum laser power needed for ignition for each specific aerosol jet velocity.

The images recoded by the digital camera showed short and bright streaks of particles crossing the laser beam. However, discrimination between the streaks produced by luminous particles that did not ignite and those that ignited and burned was ambiguous. Thus, using the PMT with a temporal resolution of 20 μs was necessary for clear identification of the ignition events. Typical examples of PMT peaks produced by different particles crossing the laser beam are shown in Figure 2.6. Figure 2.6 (a) shows a peak produced by a particle that ignited and burned. A sharp voltage rise is followed by small changes in the radiation signal occurring during the particle combustion. On the other hand, the peak shown in Figure 2.6 (b) shows the heating and cooling of the particle that never ignited, and the voltage rise is immediately followed by the voltage decrease as the particle exits from the beam. The minimum ignition threshold was established when

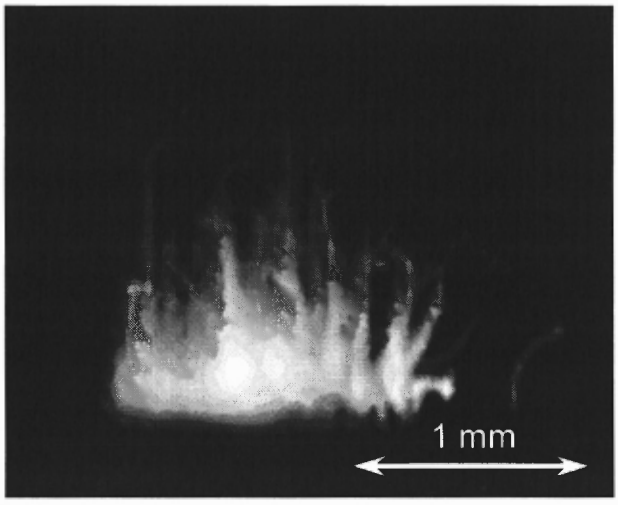

Figure 2.5 Al particle ignition and/or heating streaks captured by still camera with an 8s exposure. The aerosol jet velocity is 2.4 m/s and the laser power is 37.7 W.

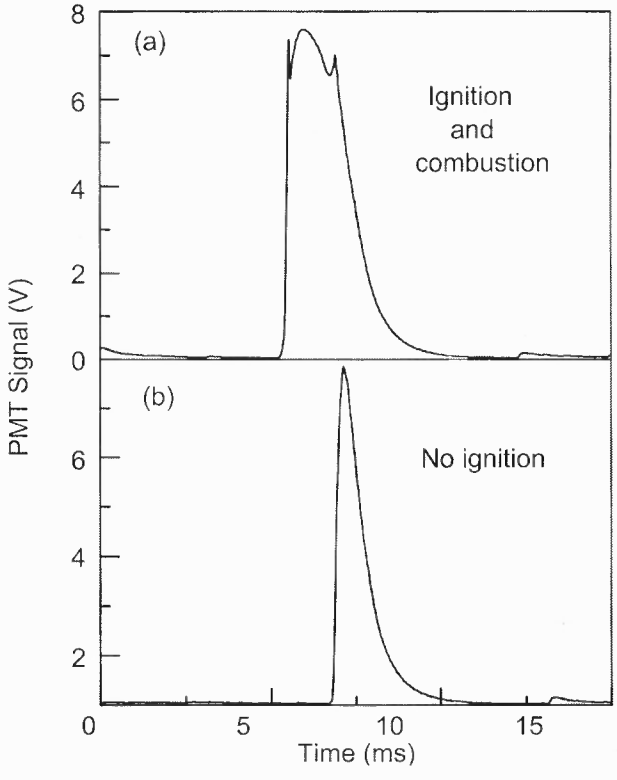

Figure 2.6 PMT signal from micron size Al particles crossing the CO2 laser beam. The aerosol jet velocity is 2.4 m/s and the laser power is 37.7 W: (a) Signal corresponding to ignition and combustion of a particle; (b) Signal corresponding to heating and cooling of an unignited particle.

at least one ignition event was detected during an 8-s period the laser was fired. The 8-s experiments were performed at least three times for each laser power setting.

The experiments were performed for three different particle velocities for any environment, so that the igniting particles were heated at three different rates. Both the jet velocity and the laser power measurements were repeated immediately before and after each ignition experiment.

2.5 Experimental Setup for Superheated Steam Environment

The setup was modified for igniting metal particles in a superheated steam environment. The modification involved connecting a steam generator and a heated delivery system to the aerosolizer. The generator produced a mixture of superheated steam and nitrogen gas at 423 K (150 °C) which was fed between the two disks comprising the top wall of the particle aerosolizer chamber, to come out as the shroud gas jet. Nitrogen was used as the central jet gas for carrying metal particles, as shown in Figure 2.7. A heated delivery system included a heated steam hose and a spiral coil heater for the top electrode of the aerosolizer. Heated path enclosure needed for the shroud flow gas channel to avoid any condensation.

It should be noted that in initial experiments, argon flow for the central jet was used. However, successful production of aerosol in the argon/steam mixture with heated components of the experimental setup could not be achieved. Indeed, the breakdown potential of argon is lower than that for nitrogen [51]; furthermore, the breakdown potential is substantially reduced at elevated temperatures [51]. Therefore, electric field

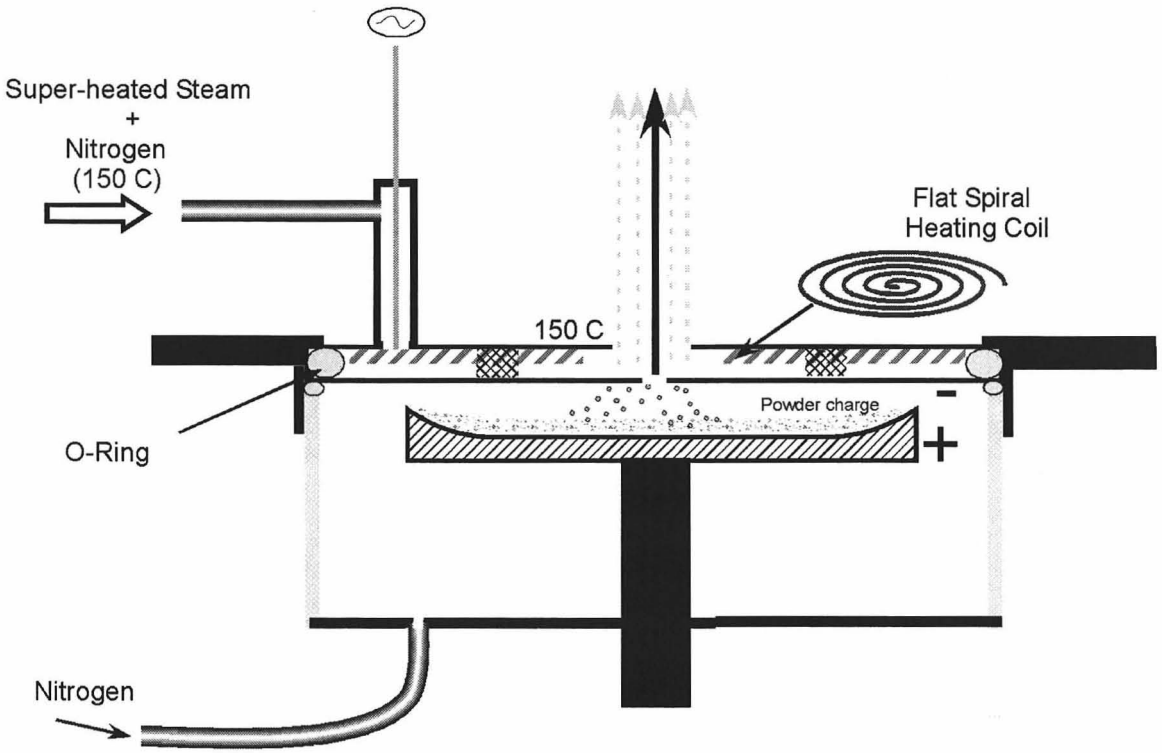

Figure 2.7 Heating coil added to experimental to allow use of steam as the shroud jet.

achievable without breakdown with argon between the plate capacitor electrodes was very low and was inadequate for aerosol jet production.

The superheated steam generator included a peristaltic pump (Variable Speed Pump by Control Company) supplying a metered amount of liquid water (typically, 0.1ml/min) into a steel tube (3.1 mm diameter, 5 m overall length) coiled inside a tube furnace (Tube Furnace 21100 by ThermoLyne). Figure 2.8 shows a schematic diagram of the steam generator. A metered nitrogen flow, measured by a gas flow meter (M-200SCCM-D by Alicat Scientific Inc.), was also fed through the coiled steel tube placed in the furnace. The nitrogen flow was necessary to maintain a smooth flow of liquid water from the peristaltic pump while ensuring its uniform boiling inside the furnace (see Figure 2.8).

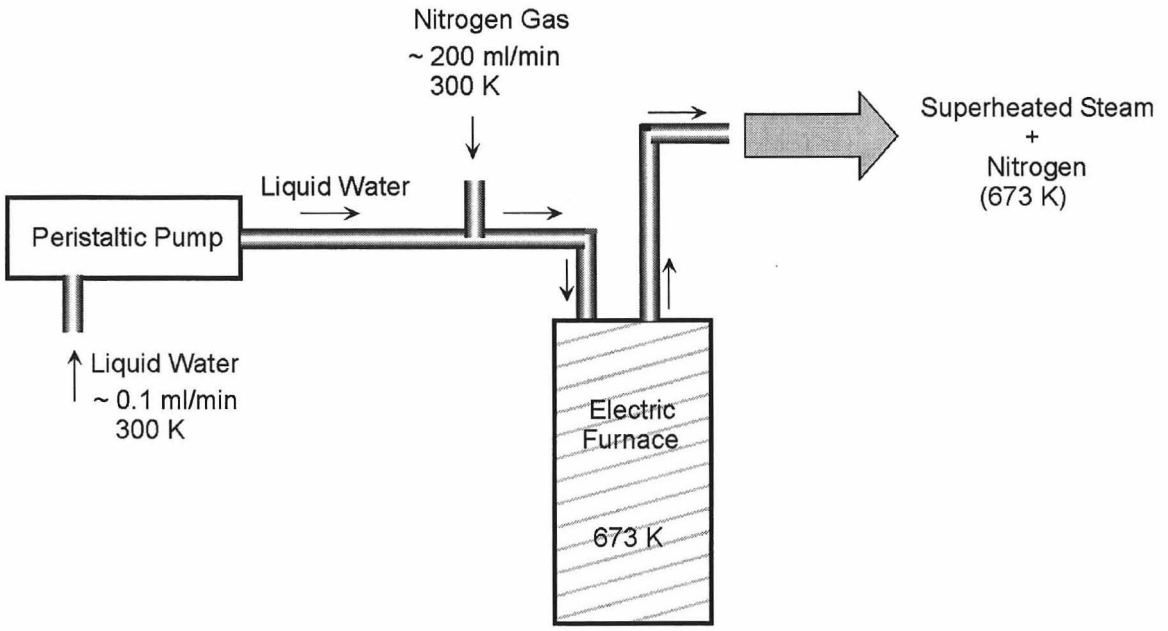

Figure 2.8 Schematic diagram of steam generator.

The furnace was pre-heated and maintained at 673 K (400 °C) to produce a mixture of a superheated steam and nitrogen gas. A heated steam hose maintained at 423 K was used to deliver the steam/nitrogen mixture to the aerosolizer.

The aerosolizer top electrode (negative) was also maintained at 423 K using a flat spiral heating coil element (coil dia.:3 in, 240V-250W, cable dia.:0.094 in, cable length: 30 in) welded between the disks of the top electrode. The superheated steam/nitrogen mixture from the heated hose is fed as the shroud jet around the central nitrogen jet carrying aerosolized particles. The top electrode also heated the nitrogen gas in the chamber to around than 423 K thus eliminating any temperature gradients between the central and shroud jets.

CHAPTER 3

HEATING OF METAL PARTICLES IN TRANSITION REGIME

3.1 Outline

This chapter deals with analysis of heating and ignition of small metallic particles in hot gases for a range of Knudsen numbers, for which the continuum description of heat transfer is not valid. A modified Fuchs' model for the transition heat transfer analysis [52] was adapted to treat diatomic gas with properties changing as a function of gas temperature. The dimensionless heat transfer coefficient, Nusselt number, was calculated as a function of particle diameter for the transition heat transfer regime. Heat transfer rates in the transition regime are somewhat different from one another for the cases of particle heating and cooling while the absolute values of the particle-gas temperature difference are the same. This effect does not exist for the continuum heat transfer model. It is observed that the applicability of the continuum heat transfer model for particles of different sizes depends on pressure and particle-air temperature difference. For example, for particles at 300 K heated in air at 2000 K, the continuum heat transfer model can be used for particle diameters greater than 10 and 1 μm at the pressures of 1 and 10 bar, respectively. Transition heat transfer model must be used for analysis of heat transfer for nano-sized particles. For calculating ignition delay in practical systems, the continuum model remains useful for particle diameters greater than 18 μm and 2 μm for 1 and 10 bar, respectively. The sensitivity of the transition heat transfer model to accommodation coefficient is evaluated. It is found that for metallic particles, accommodation coefficient has a relatively weak effect on the heat transfer rate.

3.2 Introduction

Problems involving heat transfer between spherical particles and quiescent gas are ubiquitous in such applications as laser-induced incandescence (LII) [53-55], solid propellant combustion [56-59], metal powder explosions in air [60-62], etc. Such problems also need to be considered in multiple laboratory experiments, such as powder ignition in shock tube experiments [32-36] and laser ignition of aerosol particles [63, 64]. In many cases, the particle sizes are of the order of microns and the treatment of the surrounding fluid (gas) as a continuum medium becomes invalid. Typically, transition heat transfer regime is recommended when Knudsen number, Kn, defined as $Kn = \lambda / D$, where λ is the mean free path in gas and D is particle diameter, is in the range of 0.01 – 10 [65]. Figure 3.1 shows two constant Knudsen number lines for $Kn = 0.01$ and $Kn = 10$, in the coordinates of particle diameter and temperature of air at atmospheric pressure. Conditions of heat transfer for most micron-sized particles in the applications mentioned above should be described by the transition regime.

Transition heat transfer regime has been dealt with extensively in the literature [65-67]. Various quasi-steady analytical solutions [67, 68] as well as interpolation-based approaches [69-72], describing heat transfer, have been proposed. In most of the suggested models, such as based on T-jump approximation [71] and others, a small temperature difference between particle and quiescent ambient gas is assumed. This assumption makes the respective models unacceptable for applications listed above, where a particle is typically heated to a temperature exceeding that of the surrounding gas by thousands of degrees. For a two-layer model proposed by Fuchs [73] and modified by Wright [74] the assumption of small temperature difference between the particle and gas

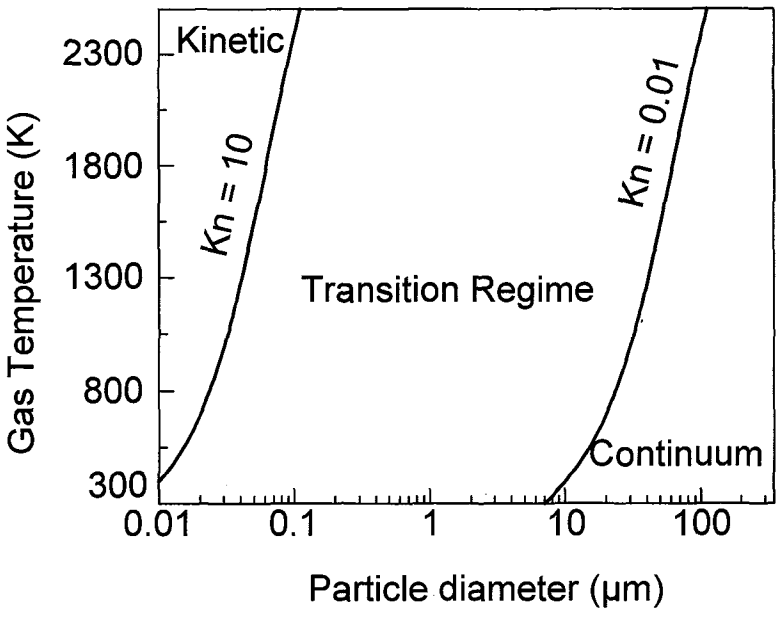

Figure 3.1 Constant Knudsen number lines as a function of particle temperature and gas temperature.

is less critical and can be relaxed. Recently, the Fuchs' model has been validated using direct Monte Carlo simulation. The model [66] has been shown to be advantageous compared to other proposed approaches [65, 66] and is recommended for use in many related applications. The model is relatively simple and readily implemented, but it still requires iterative evaluation of the temperature at the boundary between the "free-molecular layer" and "continuum" surrounding. Thus, for each specific application it is desirable to determine the range of particle sizes and experimental conditions when the use of this model is necessary. This study focuses on the applications dealing with particle ignition. In this case, the most readily detectable experimental parameter is an ignition delay for a heated particle. The discrepancy between the ignition delays predicted by the modified Fuchs model and by the continuum heat transfer calculation is determined and discussed for particles of different sizes. In addition, the version of the

Fuchs model that was validated in Ref. [66] has been further modified to account for a diatomic gas with thermal properties varied as a function of temperature. The effects of transition regime heat transfer on heating and cooling of particles of different diameters are considered and compared to each other. Finally, the sensitivity of the predicted heat transfer rate to a usually poorly known accommodation coefficient is considered.

3.3 Transition Heat Transfer Model by Fuchs Modified for Diatomic Gas

A model describing heat transfer for a sphere in transition regime was proposed by N. Fuchs [73]. The model introduced a so-called Langmuir layer with thickness δ, adjacent to the particle. The heat transfer within the Langmuir layer is assumed to occur in the free molecular regime while outside the layer, the heat transfer is described by a continuum model. The free-molecular expression for the heat transfer rate within the Langmuir layer is given as [66]:

$$\dot{q} = \dot{q}_{Free\ molecular} = \alpha\pi D^2 P_g \sqrt{\frac{k_B T_\delta}{8\pi m_g}} \frac{\gamma^* + 1}{\gamma^* - 1}\left(\frac{T_p}{T_\delta} - 1\right) \tag{3.1}$$

where α is the accommodation coefficient, m_g is the mass of a gas molecule, k_B is the Boltzmann constant, D is the particle diameter, P_g is the ambient gas pressure, T_P is the particle surface temperature, T_δ is the gas temperature at the boundary of the Langmuir layer i.e., at a distance of ($D/2$ + δ) from the center of the particle, and γ is the adiabatic index of the ambient gas. The superscript '*' indicates that the value of γ is averaged over the temperature range of (T_P - T_δ) [66], calculated as:

$$\frac{1}{\gamma^* - 1} = \frac{1}{T_P - T_\delta} \int_{T_\delta}^{T_P} \frac{dT}{\gamma - 1} \tag{3.2}$$

In the region outside the Langmuir's layer, heat transfer is calculated using the continuum regime expression [66],

$$\dot{q} = \dot{q}_{Continuum} = 4\pi\left[D/2 + \delta(T_\delta)\right]\int_{T_\delta}^{T_g} k(T)\,dT \tag{3.3}$$

where k is gas thermal conductivity. The Langmuir's layer thickness $\delta(T_\delta)$ is approximately equal to one mean free path $\lambda(T_\delta)$ [65, 74].

The value of λ is calculated for a mono-atomic gas in Ref. [66] as:

$$\lambda(T_\delta) = \frac{4}{5}\frac{k(T_\delta)}{P_g}\sqrt{\frac{m_g T_\delta}{2k_B}} \tag{3.4}$$

The effect of any pressure difference between the gas in the Langmuir's layer and the ambient gas is neglected. Note that Eq. (3.4) is different from a more general equation reported in Refs. [65, 75] and describing the mean free path in polyatomic ideal gases (see Eq. 3.5 below). Equations (3.1) and (3.3) can be solved iteratively for T_δ, so that the rate of heat transfer can be determined.

The modified Fuchs' model described above has been validated using direct Monte Carlo simulations [72] in Ref. [65, 66] for a hypothetical mono-atomic gas. In order to use this result for air, which is a diatomic gas, air properties, such as thermal conductivity and adiabatic index [76] should be used instead of the mono-atomic gas properties. In addition, Eq. (3.4) used for the mean free path calculation should be replaced by an equation appropriate for a diatomic gas. As noted above, a more generic equation for the mean free path is available and given, for example, by [65] and [75]:

$$\lambda'(T_\delta) = \frac{k(T_\delta)}{P_g}\left[\frac{\gamma(T_\delta)-1}{9\gamma(T_\delta)-5}\right]\sqrt{\frac{8\pi m_g T_\delta}{k_B}} \tag{3.5}$$

When applied to a mono-atomic gas, i.e. $\gamma = 5/3$, Eq. (3.5) is different from Eq. (3.4) by a constant factor of $\sqrt{\pi}/3$. While Eq. (3.5) allows one to account for the polyatomic gas properties depending on the specific heat ratio, γ, the direct validation of the Fuchs' model was performed in Ref. [66] using Eq. (3.4). Thus, in order to use the Fuchs' model validated in Ref. [66] to describe heat transfer in a polyatomic gas, Eq. (3.5) replaced Eq. (3.4) while being corrected by the factor of $3/\sqrt{\pi}$.

Figure 3.2 shows the dimensionless heat transfer coefficient or Nusselt number as a function of Knudsen number and as a function of the particle diameter for a selected fixed combination of particle and air temperatures. The accommodation coefficient is assumed to be equal to 1. The value of Nusselt number approaches to '2' for bigger

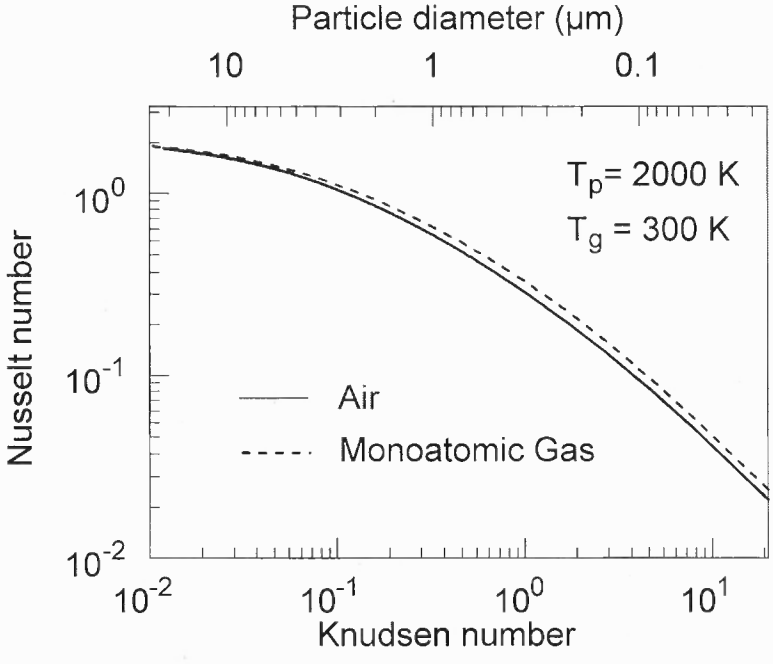

Figure 3.2 Nusselt number as a function of Knudsen number (and particle diameter) calculated for transition regime heat transfer using Fuchs' model for mono-atomic gas [66] and for air considering air properties as a function of temperature.

particles indicating the approaching continuum regime. The dashed curve is for the hypothetical mono-atomic gas used in Ref. [66]. Note that the scale is logarithmic so the difference between the curves for mono-atomic and diatomic gases is not insignificant. The Nusselt number is obtained from the calculated heat transfer rate, q.

$$Nu = \frac{q}{\pi D \bar{k} (T_p - T_g)} \tag{3.6}$$

where,

$$\bar{k} = \frac{1}{T_p - T_g} \int_{T_g}^{T_p} k(T) dT \tag{3.7}$$

In the continuum regime, heat transfer is independent of pressure. However, in transition regime analysis, the rate of heat transfer becomes a strong function of pressure. In the continuum regime, heat transfer rates are of the same magnitude for heating and cooling of a particle in hot and cold gas, respectively, when the absolute value of the particle-gas temperature difference is the same. This is no longer the case for transition and free-molecular regimes, where the magnitudes of heat transfer rates for particle heating and cooling become different even when the absolute value of the particle-gas temperature differences are the same. Indeed, the transition regime heat transfer rate depends on the Langmuir's layer thickness, δ, which is effectively equal to the mean free path at T_δ. The value of T_δ is not a simple average of the particle and gas temperatures but an iterative solution of Eq. (3.1) and (3.3) and the thicknesses of the Langmuir's layers are different for the cold and hot particles of the same sizes placed in hot and cold gases, respectively. Further, for small particles, T_δ is closer to the gas temperature than to the particle temperature, while the opposite is true for large particles. Thus, the difference between the heat transfer coefficients for heating and cooling reverses around

a specific particle size, depending on particle-gas temperatures and gas pressure. Figure 3.3 shows Nusselt number defined by Eq. (3.6) and calculated as a function of particle diameter for particle's heating and cooling in air. When a colder particle is being heated in air, for the considered air and particle temperatures, the heat transfer rate should be calculated using the Fuchs' model for particles less than about 10 and 1 μm for pressures of 1 and 10 bar, respectively. When a hotter particle is being cooled in air, the Fuchs' model should be used for particles smaller than about 50 and 5 μm for pressures of 1 and 10 bar, respectively. The above cutoff limits were calculated while allowing a 5 % deviation from the value of $Nu = 2$ corresponding to the continuum heat transfer regime. The difference between the transition and continuum heat transfer approximations is more pronounced for the particle cooling than for its heating for micron size particles and vice-versa for smaller particle sizes.

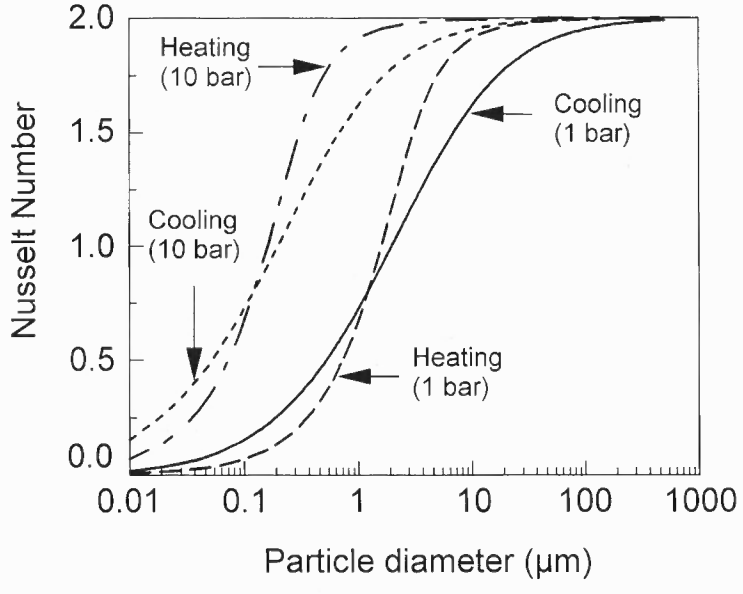

Figure 3.3 Nusselt number calculated as function of particle diameter and pressure for transition heat transfer regime at pressures of 1 and 10 bar. Particle heating: T_g=2000 K and T_p= 300K. Particle cooling: T_g = 300 K and T_p = 2000 K

3.4 Ignition Delays for Particles Heated in the Transition Regime

For many experimental situations, ignition can be modeled based on the heat balance analysis for an igniting particle. For example, for an experiment in which particles are ignited in a shock wave [32-36], the heat balance can be written as:

$$MC\frac{\partial T_p}{\partial t} = \dot{Q}_{Chemical} + \dot{Q}_{Convection} + \dot{Q}_{Radiation} \tag{3.8}$$

where M is the particle mass, C is its specific heat, and T_p is its temperature; $\dot{Q}_{Chemical}$ is the chemical heat generation rate, which is the term describing an exothermic process responsible for ignition, and $\dot{Q}_{Radiation}$ and $\dot{Q}_{Convection}$ are the radiation and convection heat transfer rates, respectively. The two latter terms can lead to the particle heating when it is below the environment temperature (and below the temperature of the surrounding walls) and to its cooling when the particle starts self-heating above the environment gas temperature due to the chemical heat generation. The radiation term is readily determined from the Stefan-Boltzmann law:

$$\dot{Q}_{Radiation} = \varepsilon\sigma_{SB}\left(\pi D^2\right)\left(T_p^{\,4} - T_w^4\right) \tag{3.9}$$

where ε is emissivity, σ_{SB} is Stefan-Boltzmann constant, and T_p and T_w are the particle and surrounding wall temperatures, respectively. It is assumed that the ambient gas temperature, T_g is equal to the wall temperature, T_g=T_w.

The convection term, $\dot{Q}_{Convection}$, is calculated using the transition regime heat transfer model described above. For comparison, the convection term is also calculated using the continuum model and neglecting particle slip, i.e., assuming that Nusselt number, Nu=2.

$$\dot{Q}_{Convection}^{continuum} = 2\pi D \int_{T_P}^{T_g} k(T)\,dT \tag{3.10}$$

The chemical heat generation rate term needs to be specifically described for each material. In this project, a simplest Arrhenius-type model was used. The specific model used in calculations was suggested for description of ignition of spherical magnesium particles [7, 58, 77]

$$\dot{Q}_{Chemical} = A_r \Delta H_{ox} \pi D^2 \exp\left[-\frac{E_a}{RT_p}\right] \tag{3.11}$$

where A_r is Arrhenius pre-exponent, A_r=10^{10} kg·m^{-2} ·s^{-1} [7], ΔH_{ox} is heat of oxidation for magnesium, E_a is activation energy, E_a= 215 kJ/mol, [7, 58, 77], and R is the universal gas constant. Note that the specific values of activation energy and pre-exponent employed here were reported in the literature based on ignition experiments for micron-sized particles. Such a description is expected to provide a reasonable accuracy for the calculations presented in this paper, while it clearly neglects the effect of transition regime heat and mass transfer processes on the rate of chemical reaction. In the future, such effect will need to be considered and a modified expression for the rate of heat generation due to chemical reaction will need to be derived.

The event of ignition was defined by the particle temperature runaway due to a rapid heat release by magnesium oxidation. Figure 3.4 shows the temperature histories predicted for a magnesium particle inserted in air at the air temperatures just below and just above the ignition threshold. Ignition delay is defined as the time required to reach the temperature runaway. When the environment temperature is below the ignition threshold, the temperature runaway is never observed.

Two parallel sets of calculations for ignition delays were performed, one using the modified Fuchs' model and the other using the continuum regime model for the heat transfer analysis. Ignition delays were calculated for magnesium particles with initial temperature of 300 K heated in a quiescent air at 2000 K. Figure 3.5 shows the ignition delays calculated as a function of particle diameter at the pressures of 1 and 10 bar. Due to a slower heat transfer predicted by the transition regime model as compared to the continuum case, much longer ignition delays are predicted for submicron sized particles heated in the transition regime. The effect diminishes as the particle size increases. The effect is also reduced for elevated pressures. It is observed that for specific air and particle temperatures considered, the continuum model can be used to predict ignition delays for particles greater than 18 and 2 μm for pressures of 1 and 10 bar, respectively.

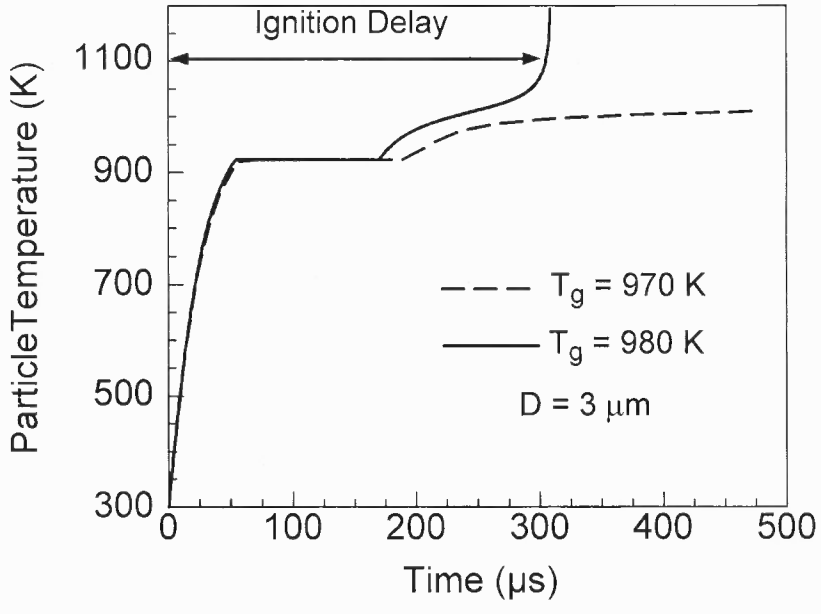

Figure 3.4 Temperature histories for Mg particle inserted in air at the air temperatures just above (solid line) and just below (dashed line) of the ignition threshold. Ignition delay is measured from time t = 0, the moment when particle is exposed to hot air.

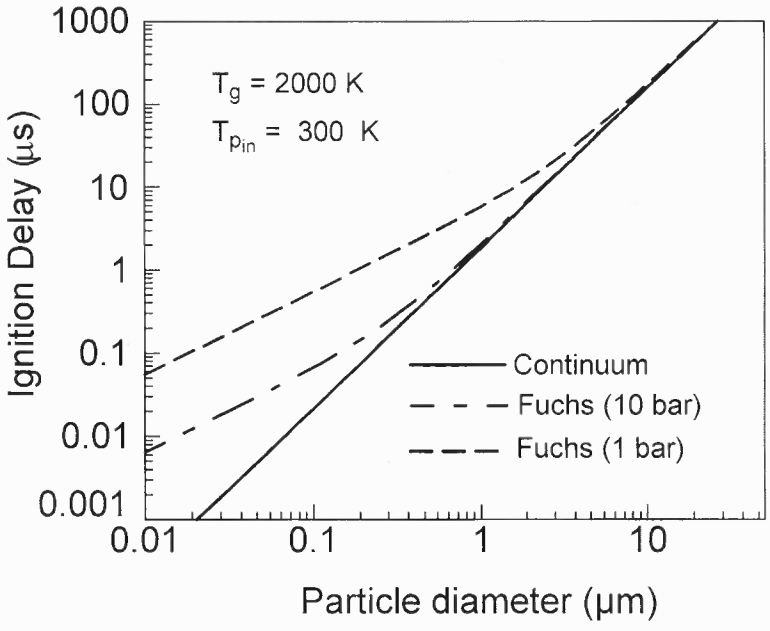

Figure 3.5 Calculated ignition delay of Mg particle at 300 K inserted in air at 2000 K as function of particle diameter and pressure.

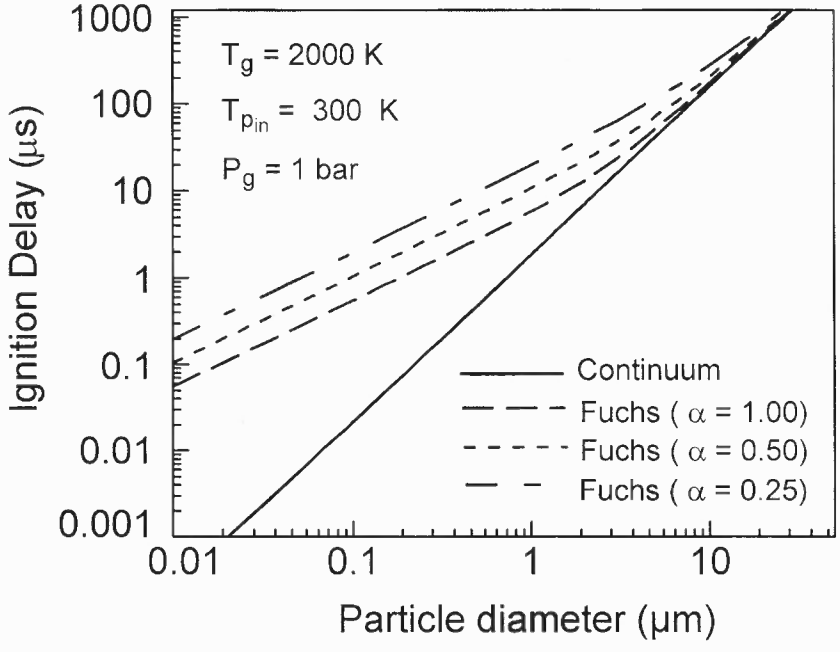

Figure 3.6: Calculated ignition delay of Mg particle at 300 K inserted in air at 2000 K as function of particle diameter and accommodation coefficient.

The particle size cutoff was calculated allowing 5% errors in the ignition delays predicted by the continuum regime calculations. Note that the ignition delay calculation considers the particle at a continuously increasing temperature. The initial part of the heating process, when the particle-gas temperature difference is the greatest, affects the predicted ignition delays most significantly.

The sensitivity of ignition delay to accommodation coefficient, α, used in describing the free molecular heat transfer in Eq. 3.1 was also considered. Figure 3.6 shows ignition delay as a function of particle diameter at air pressure of 1 bar for different accommodation coefficients. The breakdown of the continuum model occurs at larger particle diameters for smaller values of the accommodation coefficients. The accommodation coefficient for metal particles usually varies in the range of 0.5 to 0.95 [78]. Thus, according to Figure 3.6, the practical calculations of ignition delays would be relatively insensitive to uncertainties in the value of the accommodation coefficient used in the transition model.

3.5 Conclusions

The modified Fuchs' model for transition regime heat transfer was expanded to account for the properties of diatomic gases as a function of temperature. The dimensionless heat transfer coefficient, Nusselt number, was calculated as a function of particle diameter using this expanded Fuchs' model. Heat transfer rates predicted by the model are somewhat different from one another for the cases of particle heating and cooling while the absolute values of the particle-gas temperature difference are the same. This effect is not predicted by the continuum heat transfer calculations. It is observed that the

applicability of the continuum heat transfer model for description of heating or cooling of particles of different sizes depends on pressure. For processes involving particle heating by laser, particle ignition and similar processes, the continuum heat transfer model can be used for particles with diameters greater than about 10 μm at 1 bar, and for particles greater than about 1 μm at 10 bar pressure. Transition heat transfer model must always be used for analysis of heat transfer for nano-sized particles. For calculating ignition delay, the continuum model remains useful for particle diameters greater than, 18 μm and 2 μm for 1 and 10 bar, respectively. A usually poorly known accommodation coefficient is observed to have a relatively small effect on the heat transfer rate in the transition regime for metallic particles.

CHAPTER 4

MODELING: HEATING AND IGNITION OF SINGLE ALUMINUM PARTICLE WITH A CO_2 LASER IN AIR

4.1 Introduction

This chapter describes experimental results and a heat transfer model for heating and ignition of a micron sized spherical aluminum particle upon its irradiation by a focused CO_2 laser beam. The model is suitable to interpret the experimental data produced with the setup introduced in chapter 2. Heating of such small size particles in a gas should be described using transition regime heat transfer. The procedure for accounting for transition regime heat transfer described in chapter 3 has been adopted for aluminum and used here. The absorption of the CO_2 laser energy by an aluminum particle which (along with the exothermic chemical reaction) is responsible for heating the particle is also discussed. The chemical energy released by oxidation of aluminum is calculated using the alumina layer phase transformation model [27].

4.2 Experiment and Heat Transfer Model

The model calculates the temperature history of a single aluminum particle heated by a focused CO_2 laser beam. The particle is heated while crossing the laser beam, so that the characteristic particle heating times, determined by the particle speed and the beam diameter are in the range of 0.1 – 3 ms. These times are much longer than the characteristic time of temperature equilibration within the particle, $\tau \approx D^2/\alpha \sim 0.1$ μs, where D is the particle diameter and α is the metal's thermal diffusivity. Thus, the

temperature gradients within metal particles are neglected. The model considers only the particles of a selected diameter that are heated by the CO_2 laser most effectively. This diameter is determined below while analyzing the interaction of the laser irradiation with the metal particle.

Moreover, the experimental aerosol jet is assumed to be sufficiently thin to neglect the interaction between the particles. For the average feed rate of 1000 particles per second, the particles moving at about 1 m/s were separated from one another by a distance of the order of 1 mm. Because only a fraction of particles was heated by the laser and ignited, the heat transfer between the particles could safely be neglected.

The particle's temperature history is calculated using the heat balance:

$$MC\frac{\partial T_p}{\partial t} = \dot{Q}_{Laser} + \dot{Q}_{Chemical} - \dot{Q}_{Radiation} - \dot{Q}_{Convection} \tag{4.1}$$

where M is the particle mass, C is its specific heat, and T_p is its temperature; $\dot{Q}_{Laser}$ is the heat transfer rate to the particle from the laser beam, $\dot{Q}_{Chemical}$ is the chemical heat generation rate, which is the term describing an exothermic process responsible for ignition, and $\dot{Q}_{Radiation}$ and $\dot{Q}_{Convection}$ are the radiation and convection heat transfer rates, respectively. The overall goal of the proposed experimental methodology and this model is to determine the term $\dot{Q}_{Chemical}$ as a function of temperature, and thus obtain the quantitative description of the ignition kinetics. Therefore, all the other heat transfer terms must be readily calculated. The radiation term is readily determined from the Stefan-Boltzmann law:

$$\dot{Q}_{Radiation} = \varepsilon\sigma_{SB}\left(\pi D^2\right)\left(T_p^{\,4} - T_g^4\right) \tag{4.2}$$

where ε is emissivity, σ_{SB} is Stefan-Boltzmann constant, T_p and T_g are the particle and ambient air temperatures, respectively, and D is the particle diameter. The ambient air temperature is assumed to be equal to the temperature of the surrounding surfaces. The value for emissivity was selected based on the literature references [79] for aluminum surface. Note that unless specifically processed, aluminum surface is always oxidized, similar to the particles used in these experiments, validating this selection. The calculation of terms $\dot{Q}_{Convection}$ and $\dot{Q}_{Laser}$ is less straightforward. The convection term was calculated considering that for micron-sized particles, the mean free path of the gas molecules is comparable to the particle diameter. As a result, a transition regime heat transfer model based on Fuchs' model was used, as described in chapter 3. The laser absorption efficiency of the particle was estimated taking into account the absorption and scattering of the laser beam, due to the comparable particle size and laser wavelength [47, 80, 81]. A theoretical analysis describing the laser heating of micron-sized metal particles was reported in the literature [47]. However, the effects of particle melting and the specific distribution of the laser power across the beam have not been considered. The analysis presented in Refs [47, 80, 81] was reproduced and expanded in this study. The width of the laser beam was difficult to quantify experimentally with the desired accuracy and it was treated as an adjustable parameter. In order to find this parameter, aluminum particles igniting in air were considered, for which the ignition kinetics relations were reported recently [24-27]. Therefore, the term $\dot{Q}_{Chemical}$ was known so that the comparison of the ignition threshold predicted by this model to the experimentally measured threshold was used to fully define the laser heat input to the particle i.e. to quantify the diameter of the focused CO_2 laser beam. The developed model and the fully quantified

term $\dot{Q}_{Laser}$ can be used to determine the unknown $\dot{Q}_{Chemical}$ terms for different powders ignited in different environments.

4.3 Laser Heating Term

The energy distribution in the CO_2 laser beam is assumed to be Gaussian and the beam profile is considered circular. Because the laser wavelength and considered particle size are comparable, Mie's scattering theory was used to describe the laser-particle interaction. The coefficient for absorption efficiency of the laser energy by the particle is calculated as a function of the particle diameter and temperature.

4.3.1 CO_2 Laser Beam Energy Distribution

The size and profile of the CO_2 laser beam focal point is required to calculate the laser energy absorbed by the particle. Considering a particle moving in the vertical direction, along '*z-axis*', the laser power density *I(z)*, is commonly described by a Gaussian profile [82] and can be expressed as:

$$I(z) = \frac{W}{2\pi\sigma^2}\exp(-z^2/2\sigma^2) \tag{4.3}$$

where W is the total beam power and σ is the standard deviation for the beam's Gaussian function centered around $z=0$. The value of σ (or 6σ approximately equal to the beam diameter, D_{beam}) was varied as the model's adjustable parameter, as further discussed below.

Figure 4.1 illustrates quantitatively the change in the laser energy intensity experienced by a particle moving vertically, for a total beam power, W = 7.5 W and a beam diameter D_{beam} = 350 μm. The beam diameter was initially assumed to be equal to 330 μm,

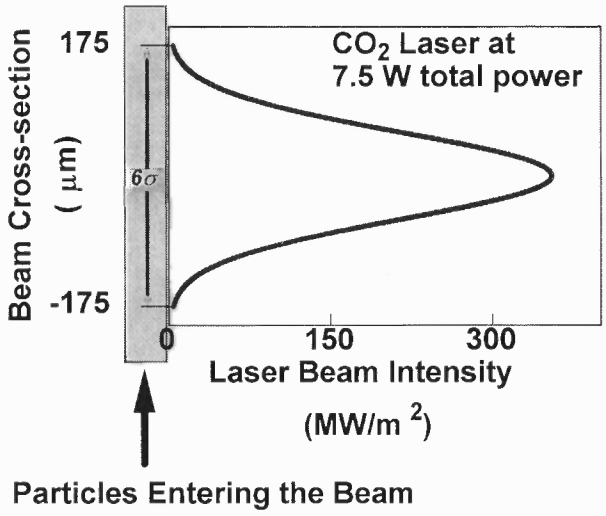

Figure 4.1 Laser energy distributions in the beam cross-section at 7.5 W of laser power for D = 350 μm

according to the measurements of the beam impression (Figure 2.4). However, the exact value of the diameter is hard to determine and this diameter was later allowed to vary as a model's adjustable parameter.

4.3.2 Absorption Efficiency

To determine the energy delivered to a particle by the laser beam, consider a particle that crosses a horizontal beam while moving along the vertical axis, z. The laser energy absorbed by the particle is a function of the particle absorption efficiency, η, and laser spatial power density $I(z)$, and can be calculated as:

$$\dot{Q}_{Laser} = \frac{1}{4}\pi D^2 \, \eta(\lambda, D, m) \, I(z) \tag{4.4}$$

where η is the particle's laser absorption efficiency depending on the laser wavelength, λ, particle diameter, D, and material's complex refractive index, m.

The laser energy absorption efficiency as a function of particle size and temperature has been described in the literature for spherical metal particles [47, 80]. The

absorption efficiency was calculated for temperatures ranging from room temperature to above particle's melting point using the Mie's scattering theory. Drude's model [47] was used to find the complex refractive index as a function of temperature.

Mie's scattering theory [47, 80] requires the complex refractive index, m, for the particle's material, which is determined from the Drude's theory [47] as:

$$m = n + ik = \left[1 - \frac{\omega_p^2}{\omega(\omega + i\gamma)}\right]^{1/2} \tag{4.5}$$

where n and k are the real and imaginary parts of m, respectively; ω is the angular frequency of incident radiation (CO_2 laser), ω_p is the plasma frequency and γ is the electron lattice collision frequency. Plasma frequency is a weak function of temperature [47] and is assumed to be independent of particle's temperature. The collision frequency changes as a function of temperature similar to the electrical resistivity of material [47, 80]:

$$\gamma = \gamma_0\left[1 + \alpha\left(T - T_0\right)\right] \tag{4.6}$$

where T_0 = 300 K, α is the temperature coefficient, and γ_0 is the collision frequency at 300 K. The values of ω_p, γ_0 and α for Al are evaluated in Ref. [47] and were reproduced here. The respective values for Mg were also calculated following Ref. [47] and using available experimental data for complex refractive index for Mg in the wavelength region of 1 - 20 μm [83], and for electrical resistivity of Mg as a function of temperature in the range of 300 - 3000 K [79]. The final parameters used in the model are listed in Table 4.1.

Once the complex refractive indices are found, the absorption efficiency is calculated as a function of the particle diameter and temperature using Mie's scattering

Table 4.1 Drude's Theory Parameters Used to Calculate the Complex Refractive Index [47]

Parameters	*Al*	*Mg*
Plasma Frequency ω_p (s^{-1})	$1.89 \cdot 10^{16}$	$1.15 \cdot 10^{16}$
Collision Frequency γ_0 (s^{-1})	$1.13 \cdot 10^{14}$	$2.58 \cdot 10^{14}$
Temperature Coefficient, α (K^{-1})	$4.5 \cdot 10^{-3}$	$4.0 \cdot 10^{-3}$

theory, as described in Ref. [47, 80]. A brief description is presented below.

The absorption efficiency based on cross-section can be defined as,

$$Q_a = C_a / (\pi D^2 / 4) \tag{4.7}$$

where D is particle diameter and,

$$C_a = \frac{\lambda^2}{2\pi} \sum_{j=1}^{\infty} (2j+1)[\mathrm{Re}(a_j + b_j) - (|a_j|^2 + |b_j|^2) \tag{4.8}$$

where

$$\begin{aligned} a_j &= \frac{[\Lambda_j(mx)/m + j/x]\psi_j(x) - \psi_{j-1}(x)]}{[\Lambda_j(mx)/m + j/x]\xi_j(x) - \xi_{j-1}(x)]} \\ b_j &= \frac{[m\Lambda_j(mx) + j/x]\psi_j(x) - \psi_{j-1}(x)]}{[m\Lambda_j(mx) + j/x]\xi_j(x) - \xi_{j-1}(x)]} \end{aligned} \tag{4.9}$$

$$x = \pi D / \lambda = SizeParameter \tag{4.10}$$

Symbol ' Λ ' indicates logarithmic derivative. 'a' and 'b' are the absorption coefficients and form a converging series. The absorption coefficients are calculated using steps described in appendix 'A' of Bhormen and Huffman [80]. The value of the coefficient decreases rapidly and only first few terms (q_2) contribute to the value of the absorption cross-section. The number of significant terms can be estimated as

$$q_2 = (x + (4x^{1/3} + 2)) \tag{4.11}$$

ψ_j and ξ_j are Bessel functions satisfying recurrence relation and are calculated by upward recurrence using following relations,

$$\psi_{j+1}(x) = \frac{2j+1}{x}\psi_j(x) - \psi_{j-1}(x) \tag{4.12}$$

$$\xi_j = \psi_j - i\chi_j \tag{4.13}$$

$$\psi_{-1}(x) = \cos(x), \psi_0(x) = \sin(x) \tag{4.14}$$

$$\chi_{-1}(x) = -\sin(x), \chi_0(x) = \cos(x) \tag{4.15}$$

The logarithmic derivative 'Λ' in the expressions for 'a' and 'b' satisfies the following recurrence relation and is calculated using backward recurrence.

$$\Lambda_{n-1} = \frac{j}{mx} - \frac{1}{\Lambda_j + j/mx} \tag{4.16}$$

where,

$$\Lambda_{q_1} = 0 + i0 \tag{4.17}$$

and

$$q_1 = \max(q_2, |mx|) + 15 \tag{4.18}$$

Figure 4.2 shows the absorption efficiency for aluminum as a function of particle diameter presented in the literature [47] and reproduced in this study. Similar calculations were also performed for magnesium. The results are presented in Figure 4.3. It was observed that for a specific laser wavelength (10.6 μm for CO_2 laser), the absorption efficiency peaks at the same particle size ($D \approx 3.37$ μm) for different metals. Because of this particle size selective heating, only the particles with the peak absorption efficiency ignite at the threshold laser power in the present experimental methodology. In practical

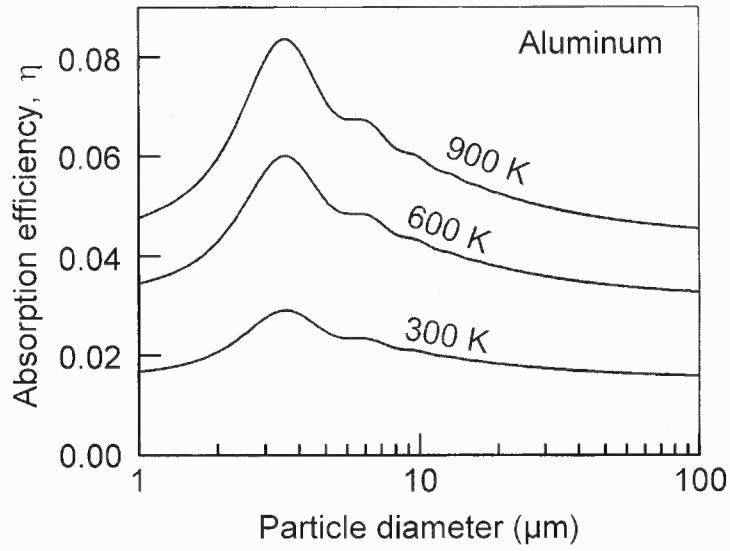

Figure 4.2 CO_2 laser beam absorption efficiency as a function of aluminum particle size for different temperatures. The results are obtained in this work and reproduce the data reported earlier [47]. The peak efficiency occurs for the metallic particle diameter of 3.37 μm, nearly independently of material.

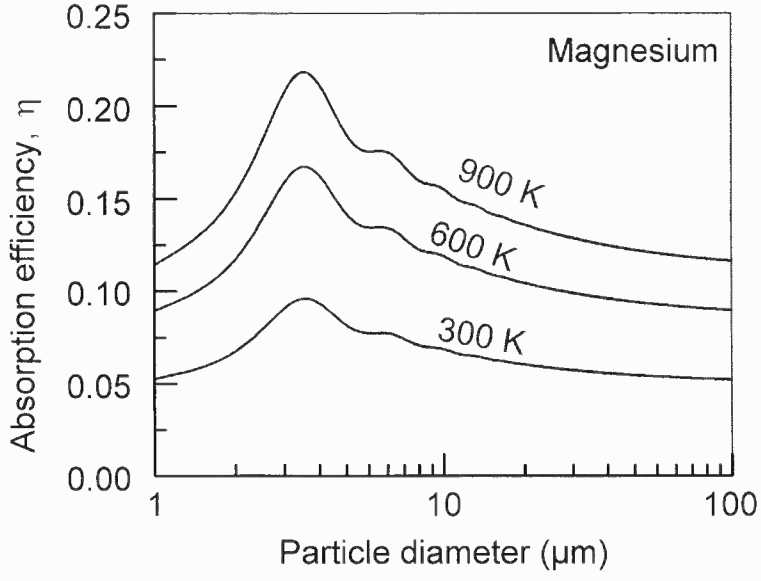

Figure 4.3 CO_2 laser beam absorption efficiency as a function of magnesium particle size for different temperatures. The peak efficiency occurs for the metallic particle diameter of 3.37 μm.

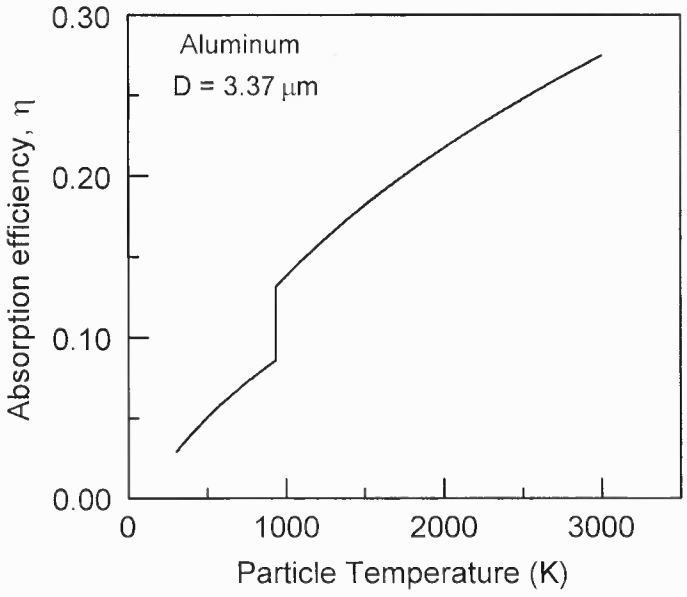

Figure 4.4 CO_2 laser beam absorption efficiency as a function of aluminum particle temperature. The jump occurring upon melting is described in Ref. [81].

terms, estimates showed that the experimental error in the laser power will lead toignition of particles within a size range of about 3.3 – 5 μm.

The model was modified to take into account the melting effect on the absorption efficiency [81]. On melting, the particle density changes abruptly [79] and the absorption efficiency experiences a jump as shown in Figure 4.4. The overall absorption efficiency for a particle undergoing melting was calculated as a weighted average of the efficiencies for its solid and liquid parts.

4.4 Convection Term

For a 3.4 μm diameter particle in an atmospheric pressure air at room temperature, the value of Knudsen number (Kn) is close to 0.03. The conventional, continuum convection model is only valid for Kn<0.01, and at greater values of Kn, a transition model needs to be considered. The correction for the dimensionless heat transfer coefficient or Nusselt

number (Nu) is described in chapter 3, as shown in Figure 3.2, for a specific combination of the particle and gas temperatures as relevant to this work. It is clear that the correction is significant compared to Nu≈2 for continuum heat transfer. Properties of dry air [16] including the adiabatic index, γ, and thermal conductivity, k_g, were used. An accommodation coefficient of A = 0.87 for Al particle [78] was used. Literature data summarized in Ref. [78] indicate that the accommodation coefficient for Al can vary in the range of 0.87 – 0.97 depending on the surface finish and etching. The value selected in this project is for a clean, un-etched surface that is normally expected to be coated with alumina.

4.5 Chemical Term

For Al powder used in the experiments, the ignition model described recently [24-27] was used. The model calculates the rate of oxidation that is limited by the rate of transport of oxygen or aluminum through the protective surface oxide layer. It has been reported that aluminum powders are coated with a 2.5-nm thick layer of amorphous alumina [42-45] which was the assumed initial oxide coating in the model. As the particle temperature increases, different polymorphs of Al_2O_3 become stable [24,46] and the model considers the kinetics of respective polymorphic phase transitions. The transformations accompanied by significant increase in density of alumina, such as amorphous to γ-alumina and γ- to α alumina can also be accompanied by disruptions in continuity of the protective oxide. Thus, the oxidation rates and respective heat release rates are predicted to increase rapidly when such phase changes occur. Further details of the oxidation model for aluminum particles are available in Ref.[27]. The model was developed for

aluminum ignition in air [24-27]. Therefore, it is acceptable for description of the present experiments in which aluminum ignition in air is being considered.

4.6 Results and Discussion

The model was used to predict the temperature history for a particle crossing a laser beam. The calculations were performed for different particle velocities, corresponding to the experimental aerosol jet velocities. For each calculation, the laser power was allowed to vary to find the threshold power at which ignition was predicted to occur. Figure 4.5 shows calculated Al particle temperature histories at three different particle velocities. The dashed curves show the particle temperatures when the laser power is just under the ignition threshold.

The heating up and cooling down parts of the curves correspond to the particle's entrance to and exit from the laser beam. The solid curves, showing the particle temperature histories at the threshold power, are closely following the dashed curves during the initial heating period. The curves diverge as the particle temperature increases and the role of term $\dot{Q}_{Chemical}$ becomes increasingly significant.

The calculations were performed until the particle temperature reached the alumina melting point of 2320 K. Above this temperature, the analysis of heterogeneous processes rate limited by diffusion through the oxide layer may no longer be relevant. Furthermore, the oxide coating can no longer remain protective and so the particles reaching this temperature considered ignited.

Three cases illustrated in Figure 4.5 correspond to different heating rates (or different velocities at which the particles crossed the laser beam.) It is clear that at lower

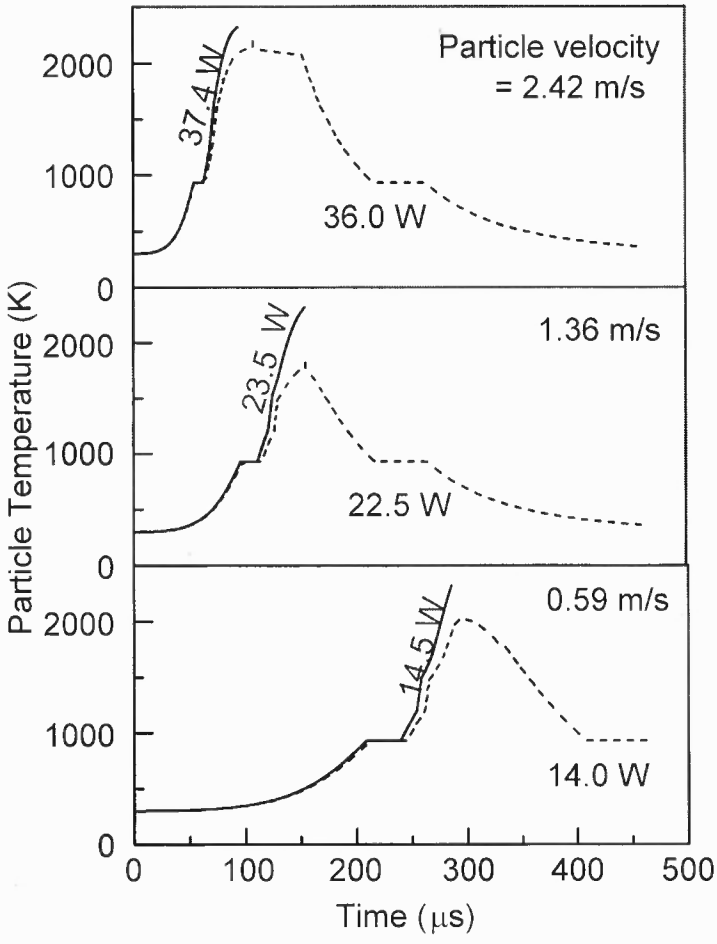

Figure 4.5 Temperature histories for laser-heated 3.37 μm diameters Al particles calculated for three different particle velocities. The dashed lines show the cases when the laser power is just below the ignition threshold and the solid lines show the cases with the laser power at the threshold.

heating rates, the predicted ignition threshold laser power is also lower.

A comparison between different terms in the energy equation, Eq.(4.1) is shown in Figure 4.6 for a case of a particle crossing the laser beam at 0.59 m/s and the laser power set at 14.5 W. Radiation heat losses are insignificant and are always less than 1 % of the laser heat input. Therefore, the specific choice of particle emissivity, which is poorly known for oxidized Al surface, is not important. Convection heat losses represent the dominant heat removal mechanism for the particle. The chemical heat input comes

into play and becomes noticeable only after the particle reaches a certain temperature. A sharp increase in the chemical heat generation after the melting plateau is due to a very rapid reaction controlled by the gas phase diffusion to the portion of Al surface exposed to air after the phase transformation from amorphous to gamma alumina polymorph [24-27]. Once the openings in the newly formed gamma oxide heal, the reaction starts to be controlled by the condensed phase diffusion producing a sudden decrease in the rate of chemical heat generation [24, 25].

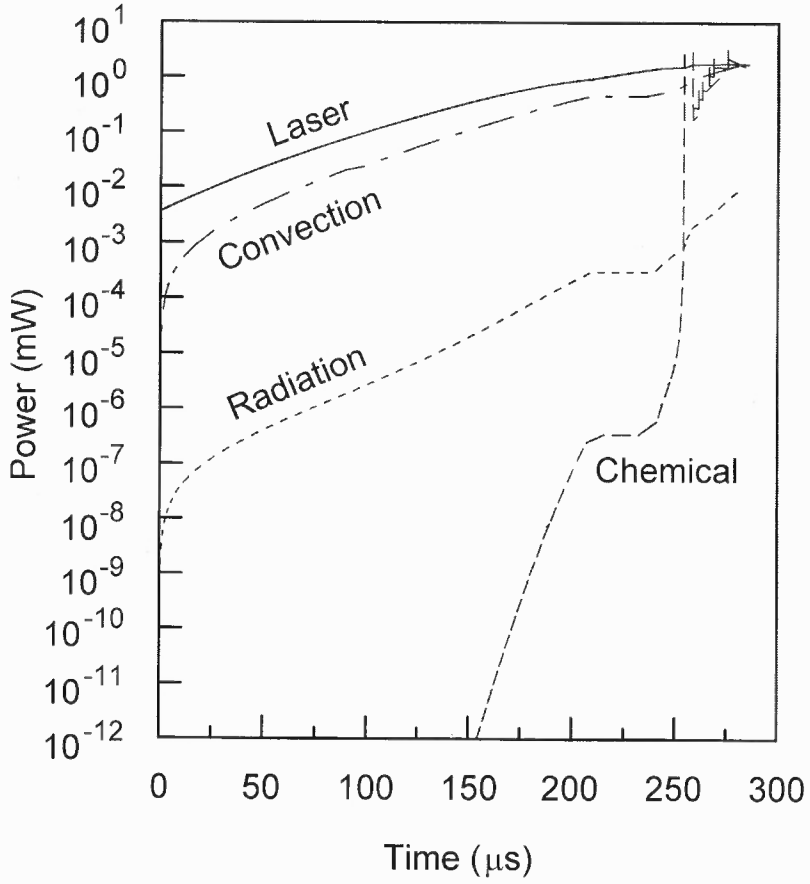

Figure 4.6 Different terms of the energy equation, Eq. (4.1) for an Al particle of 3.37 μm diameter crossing a CO_2 laser beam, set at 14.5 W, at 0.59 m/s.

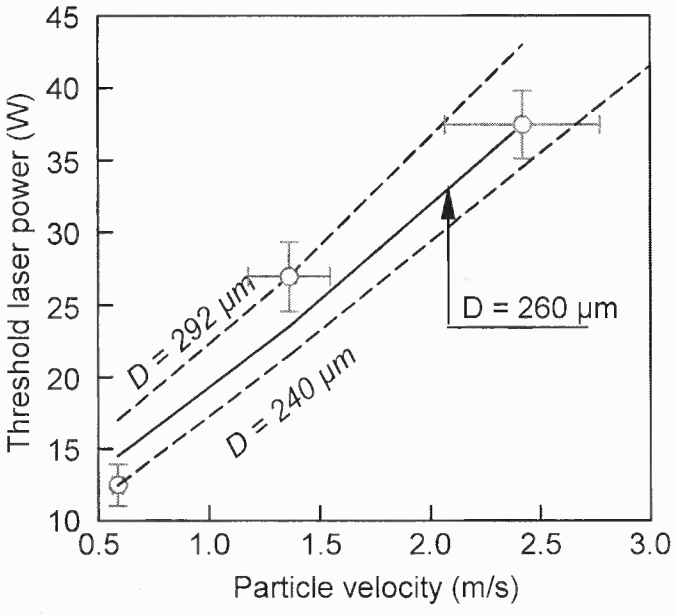

Figure 4.7 Experimental results and calculated laser power thresholds for ignition of Al particles for different particle velocities (at different heating rates). Each line is calculated by selecting $6\sigma \approx D_{beam}$ to match one of the experimental points.

Experimental laser power thresholds for ignition of Al powder at three different particle velocities are shown in Figure 4.7. The powder ignited at 14.5 W, 23.5 W, and 37.4 W for the particle velocities of 0.59 m/s, 1.37 m/s, and 2.42 m/s respectively. For each pre-set laser power level, the ignition was detected optically, using the PMT ignition peaks. At the threshold power, at least one particle was observed to ignite during a period of 8 second. This ignition statistics is reasonable considering a small number of particles with diameters in the range of 3.3 - 5 μm among poly-dispersed aluminum particles fed into the aerosol jet. In addition, only a fraction of particles in the jet crossed the laser beam close to its centerline while the particles crossing the beam at its periphery were heated to a much lower temperature. The error bars for the threshold laser power show the step size used to adjust the laser power experimentally as well as the experimental error in the laser power setting. The error bars shown for the particle

velocities represent the standard deviation for the velocity measurements based on the multiple recorded particle streaks.

The adjustable parameter, 6σ, describing the width of the Gaussian profile for the energy distribution across the laser beam was varied between 240 μm and 292 μm to match the experimental laser threshold powers at different heating rates. For each measured threshold laser power corresponding to a specific heating rate, the value of 6σ was found at which the predicted laser power matched the experiment. This value was then used to predict the laser threshold powers for the entire range of heating rates used in experiments. Thus, the three resulting calculated lines are shown in Figure 9; each line, as described above, was selected to match one of the experimental points exactly. Most importantly, for all three cases the overall predicted dependencies of the laser threshold power on the heating rate (or particle velocity) match well the experimental trend. The value of $6\sigma = 260$ μm, selected for the laser threshold power at the highest heating rate, appears to match the experimental points at different heating rates best and is considered as the final selection for the model's adjustable parameter.

The developed model describes the experiment adequately and the calibrated heat transfer term describing the CO_2 laser heating of metallic particles can now be used to determine the unknown ignition kinetics for powders other than spherical aluminum used in these experiments. Alternatively, the same methodology can be used to determine the kinetics of aluminum ignition in environments other than air. The unknown term $\dot{Q}_{Chemical}$ can be found by matching the experimental and calculated trends for the laser power ignition threshold as a function of the heating rate and using the terms $\dot{Q}_{Laser}$, $\dot{Q}_{Radiation}$, and $\dot{Q}_{Convection}$ determined above.

4.7 Summary

Heat transfer model was developed to interpret result produced by the experiment described in chapter 2. The developed heat transfer model includes radiation, convection in the transition regime, and a detailed analysis of the heat transfer from a laser beam to metal particles. Transition regime heat transfer described in Chapter 3 was used to estimate convective heat loss from the particle to surrounding environment. Absorption of laser energy by the particle was calculated using Mie's scattering theory. The model considered heating rates on the order of 10^6 K/s achieved in the experiment, which are close to those occurring in many practical applications of metal-containing energetic materials. Because the experiment uses a CO_2 laser to heat micron-sized metallic particles, which are comparable to the laser beam wavelength, the heating is most efficient for the particles of a specific diameter, close to 3.37 μm. This particle size-selective heating simplifies dramatically the theoretical analysis of the heat transfer while allowing one to use regular poly-dispersed powders in experiments. The model was calibrated comparing the calculations and experimental data acquired for spherical Al particles, for which the ignition kinetics parameters were determined elsewhere. The developed experimental technique and the heat transfer model enable one to quantify the kinetics of ignition of a metallic particle in a gaseous environment of interest. The heat transfer term describing the unknown ignition kinetics can be determined by matching the experimental and predicted laser power thresholds necessary for particle ignition at different velocities at which the particles cross the laser beam and, therefore, for different heating rates.

CHAPTER 5

ALUMINUM PARTICLE IGNITION IN DIFFERENT OXIDIZING ENVIRONMENTS

5.1 Introduction

Aluminum powder is widely used as a fuel additive in solid propellants, explosives, and pyrotechnics. Ignition and combustion of aluminum particles have been extensively studied in the past but many of the related processes are not understood sufficiently well to enable their quantitative modeling. Currently, research of aluminum ignition and combustion in various configurations is very active involving both experimental [25, 84 – 86] and modeling [27, 87, 88] efforts. Quantitative description of particle ignition processes is of specific importance for the practical applications, in which such processes determine ignition delays and bulk burn rates for aluminum. As described in section 4.5, an ignition model for aluminum particle in oxygen was suggested based on detailed thermo gravimetric (TG) studies of aluminum powders oxidation [27]. Oxidation was established to occur in several steps, including growth of the initial amorphous oxide layer, a phase change from the amorphous to γ-Al_2O_3 polymorph accompanied by an increase in the oxide density and formation of discontinuities in a thin alumina scale, growth of γ-Al_2O_3 and its transformations into θ- and later α-Al_2O_3 polymorphs. Each alumina polymorph presents a specific diffusion resistance and thus is oxidized at a specific rate. The polymorphic phase transition result in stepwise changes in the oxidation rate. The rates of mass transfer processes accompanying oxidation of different alumina polymorphs and rates of polymorphic phase changes occurring in alumina were

quantified based on the TG measurements [25]. Combining the quantitative description of heterogeneous oxidation processes with the heat transfer analysis for aluminum particles introduced in a hot gas environment or heated by another source (e.g., laser beam) enables one to predict the ignition delay as a function of the particle size and external conditions. The model was validated experimentally for the aluminum particles rapidly heated and ignited in the CO_2 laser beam in air [8], described in Chapter 4.

However, in many practical applications oxygen is not the primary oxidizer available for the ignition of aluminum powders. Instead, ignition occurs in CO_2 and H_2O environments [89, 90]. This chapter deals with experimental study of ignition of aluminum particles heated rapidly in well-controlled environments with H_2O and CO_2 being the primary oxidizers. The laser ignition experimental methodology is similar to that for ignition experiments in air as described in Chapter 4. The experimental setup is modified (see section 2.5) to enable studies of aluminum ignition in water vapor, carbon dioxide, and mixed oxidizers.

5.2 Experimental Approach and Apparatus

This set of experiments is aimed to understand thermal ignition of aluminum particles in different environments. The experimental approach is similar to the earlier experiments conducted in air. Threshold CO_2 laser power required to ignite a particle is measured for a set of particle jet velocities in different gas environments. The experimental setup is described in detail in Chapter 2. Figure 2.1 includes an aerosol jet generator, a 125 W CO_2 laser (by Synrad, Evolution 125 series) with a ZnSe convex lens (0.75″ aperture and 4″ focal length), and a modulated green laser (SUWTECH model DPGL-3000 by Photop

Technologies, Inc) operated with a set of a semi-cylindrical and convex glass lenses to produce a laser sheet for the jet visualization. In these experiments a more sensitive photomultiplier tube (PMT) by Hamamatsu (model PMT C7247) was used to measure emission traces of the heated and ignited particles.

In experiments involving H_2O, superheated steam was generated using a customized superheated steam generator as described in section 2.5.

For experiments with CO_2 serving as an oxidizer, the shroud gas was pure CO_2 and the heaters for hoses and components of the aerosol generator were turned off. CO_2 was also used as the central jet carrier gas. For mixed CO_2/O_2 environments, a premixed CO_2/O_2 mixture was used for both shroud and central gas flows.

5.3 Simulation of Gas Mixing for Ignition Experiments

A numerical simulation was used to establish the gas concentrations in the mixed flows used in experiments. Gambit, a pre-processing software, was used to model the geometry of the aerosol generator outlet. Experimental geometry of the central jet nozzle and the shroud flow nozzle was directly introduced into the code. An axisymmetric cylindrical geometry for the jet was considered. For the calculations, the space was covered by 2 different meshes. Both meshes used quadrilateral elements. The first, internal mesh had a relatively small node-to-node distance of 0.1 mm. It was used in the central zone where the jets were produced and where the concentration gradients were likely to be high. The second, external mesh had a 5 mm distance between nodes, and was used for the ambient gas. Computational fluid dynamic (CFD) code Fluent was used for numerical calculations. Calculations assumed laminar gas flow and considered a gas jet neglecting

the presence of particles. This analysis describes the experiments well considering the very low particle number densities used.

The gases were introduced into the system using mass flow inlets, corresponding to the mass flow rate measurements obtained in experiments. The heat transfer to the walls was neglected and walls were assumed to be at the same temperature as the adjacent gas elements.

The results of calculations for a specific case are presented for example in Figures. 5.1 and 5.2. These calculations used a N_2 flow rate of 100 ml/min at 293 K in

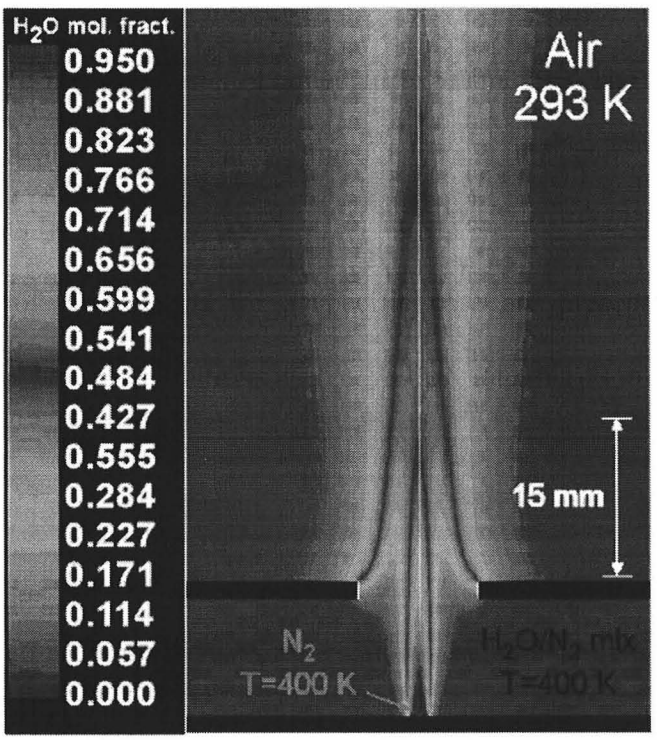

Figure 5.1 Mole fraction of water as a function of vertical and horizontal coordinates for the produced mixed jet. The specific conditions are: Flow rate of N_2 (central jet): 100 ml/min at 293 K; Flow rates of H_2O/N_2 mixture represent 100 ml/min of N_2 at 293 K and 0.085 ml/min of liquid water. Temperature of all entering gases is 400 K. The final mixture consists of 57.5 mass % of N_2 and 42.5 mass % of H_2O. The environment is air at 293 K.

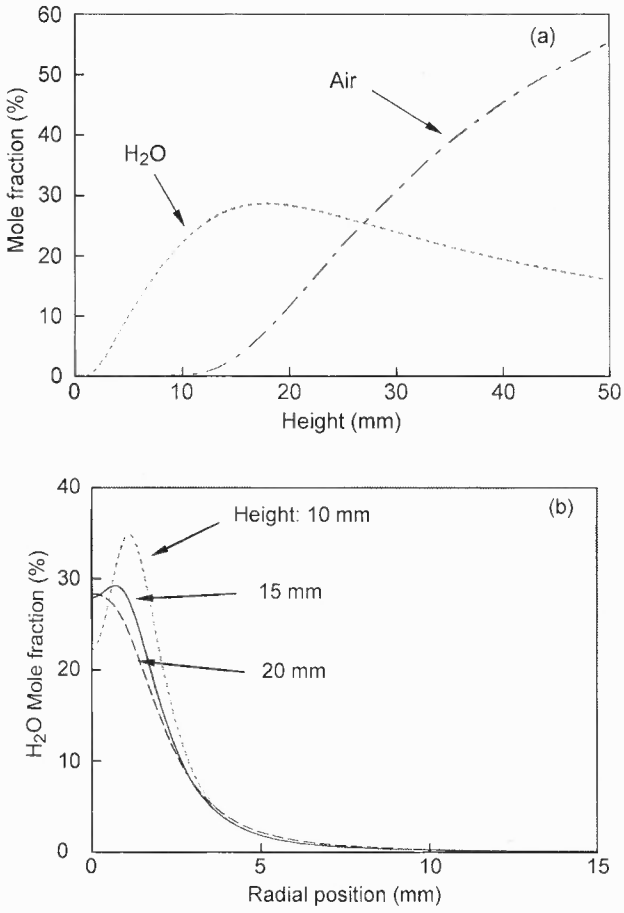

Figure 5.2 Concentration profiles for flow conditions presented in Figure 5.1; (a) H_2O and air mole fraction along the jet's axis; (b) H_2O mole fraction at radial positions away from the jet axis.

the central jet and a mixture of H_2O/N_2 comprising of 0.085 ml/min of liquid H_2O and 100 ml/min of N_2 at 293 K in the shroud jet. These conditions are representative of those used in experiments. Temperature of all entering gases is 400 K. The final mixture consists of 57.5 mass % of N_2 and 42.5 mass % of H_2O. The environment is air at 293 K. The environment along the axis of the jet is stable after around 10 mm from the jet exit. The laser spot was focused at the jet 12 mm above the nozzle. These calculations were

used to find out region with stable mixture environment and exact composition of mixture at the laser focal spot.

Figure 5.1 shows that mixing of the starting H_2O/N_2 gas coming as a shroud jet with the central nitrogen jet is nearly completed about 1 cm above the nozzle and that the water concentration across the jet is nearly uniform at the location of the laser beam (about 1 cm above the shroud nozzle). The specific water concentration present at that location is important for further analysis of the experimental results.

Mole fraction profiles for H_2O and air are shown in Fig. 5.2 (a). There is effectively no contamination of surrounding air up to 12 mm along the jet axis. The CO_2 laser was always focused within this region. Figure 5.2 (b) shows H_2O mole fraction at positions radially away from the jet axis. H_2O concentration is stable within 2-3 mm of the jet axis which is more than the width of the jet.

Using the Fluent calculations, each of the experimental conditions shown in Table 1 was described.

Table 5.1 Volumetric Composition (%) of Gases at Laser Focal Spot in Different Environments

Environments	*N_2*	*O_2*	*CO_2*	*H_2O*	*Central Jet Feed*	*Shroud Jet Feed*
Air	79	21	-	-	Air	Air
H_2O / N_2	65	-	-	35	N_2	H_2O / N_2
H_2O / Air	51	14	-	35	Air	H_2O / Air
CO_2	-	-	100	-	CO_2	CO_2
CO_2 / O_2	-	21	79	-	CO_2 / O_2	CO_2 / O_2

5.4 Material

Aluminum powder, spherical, 99% pure by Alfa Aesar with nominal average particle size of 4.5 – 7 μm was used in this study. Figure 5.3 shows the particle size distribution of the powder as measured by laser diffraction technique (Beckman Coulter LS-230). Note that while the particle size distribution does not peak around 3.4 μm (the particle size heated by the CO_2 laser most effectively), the number of particles with this size is substantial.

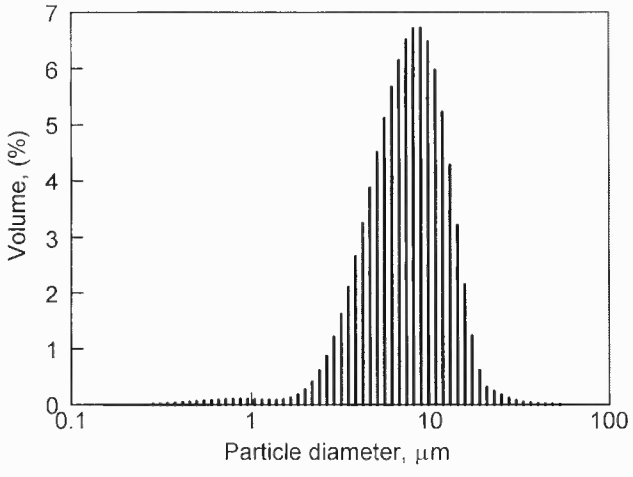

Figure 5.3 Particle size distribution of spherical aluminum powder, 99% pure aluminum by Alfa Aesar with nominal average particle size of 4.5 – 7 μm, measured by Coulter LS-230.

5.5 Experimental Procedure and Data Analysis

Experimental gas environments were produced as shown in Table 5.1. Threshold CO_2 laser power required for particle ignition was measured for three different velocities for each environment, similar to the experiments in air described in Chapter 4. The aerosol jet velocity was measured using particle image velocimetry, with a modulated green laser with modulation frequency in the range of 300 to 3000 Hz, with the higher frequencies

selected for higher jet speeds. Produced particle streaks were recorded using the digital camera and the streak lengths were measured to determine the jet velocity.

The CO_2 laser was focused about 1 cm above the jet nozzle using an auxiliary red laser aligned with the CO_2 laser beam and the ZnSe lens. Once a stable aerosol jet was established, the CO_2 laser was fired continuously for 8 seconds, at a preset power level. Visible radiation generated by heating and/or ignition of particles was monitored using a PMT connected to a PC-based data acquisition system. The experiment was repeated with the laser powers gradually increased until ignition events were clearly detected. Each set of experiments was repeated at least three times.

Two approaches were combined to detect particle ignition. The first approach is based on the shapes of particle emission pulses as used in experiments in Chapter 4. Figure 5.4 shows typical examples of the recorded PMT output pulses produced by particles crossing the CO_2 laser beam (39.3 W) in air environment at a speed of 2.63 m/s. The peak shape on the left indicates ignition and combustion event while the smooth peak shape on the right implies the particle being heated by the laser without ignition. The minimum ignition threshold was determined if at least one ignition event was detected during an 8-s period the laser was fired. For each laser power setting the laser was fired three times for 8 s. The laser power setting is assumed to ignite the powder if ignition event is observed in all three 8 s runs. The measurements for both the jet velocity and the laser power were made immediately before each ignition experiment. In the second approach, in addition to peak shape analysis, the PMT peak data were also analyzed statistically for the peak width of the ignition/heating pulses to ascertain the ignition event. Figure 5.5 shows the frequency distribution of peak widths of pulses accumulated

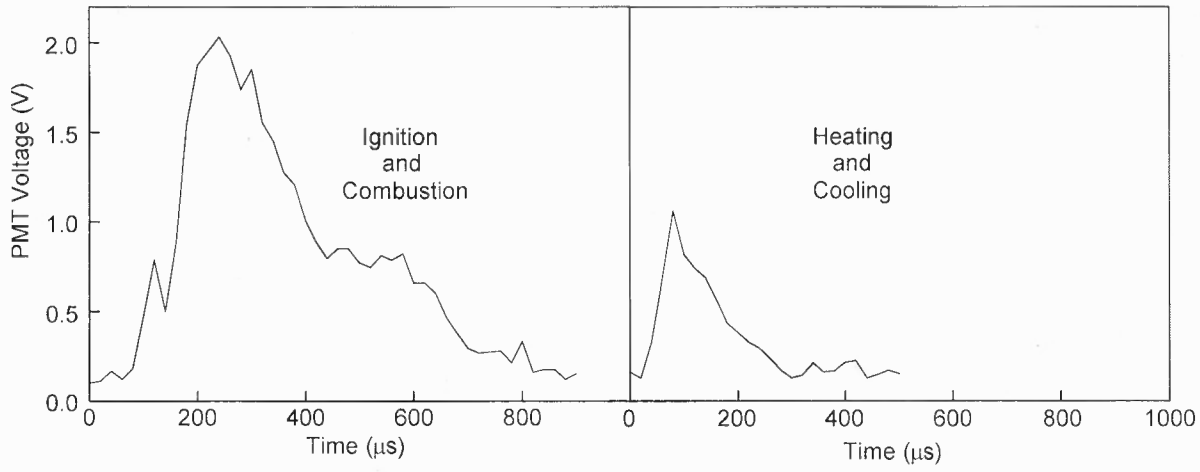

Figure 5.4 Typical examples of PMT signals recorded for Al particles in air crossing the CO_2 laser beam (at 39.3 W) in air environment at a speed of 2.63 m/s. The heating and cooling of the un-ignited particles in the laser beam produces a narrow peak without a plateau or an extended period corresponding to the particle combustion.

during 24 s (three 8-s runs) for different CO_2 laser powers at the fixed jet velocity of 1.5 m/s in air. The peak shape analysis for this experiment gives the threshold laser power to be at 20 W (between 18.1 and 21.9 W). As can be seen from Figure 5.5, only a very few narrow peaks are detected at the laser power of 12.1 W. Increase in the laser power to 14.8 W produces greater number of peaks and the peak widths begin forming a distribution around 300 μs. In the first approach of signal processing described above, these peaks were attributed to un-ignited particles heated in the laser beam, based on their characteristic peak shape shown on the right in Figure 5.4. Upon further increase in the laser power to 18.1 W, peaks with substantially greater durations around 900 μs first appear as a tail of the peak widths distribution. The shapes of these wider peaks are similar to that shown on the left of Figure 5.4. These wider peaks are attributed to igniting particles. Thus, for the example shown in Figure 5.5, based on the peak width statistical distribution, the ignition threshold is detected at 18.1 W and the peak shape

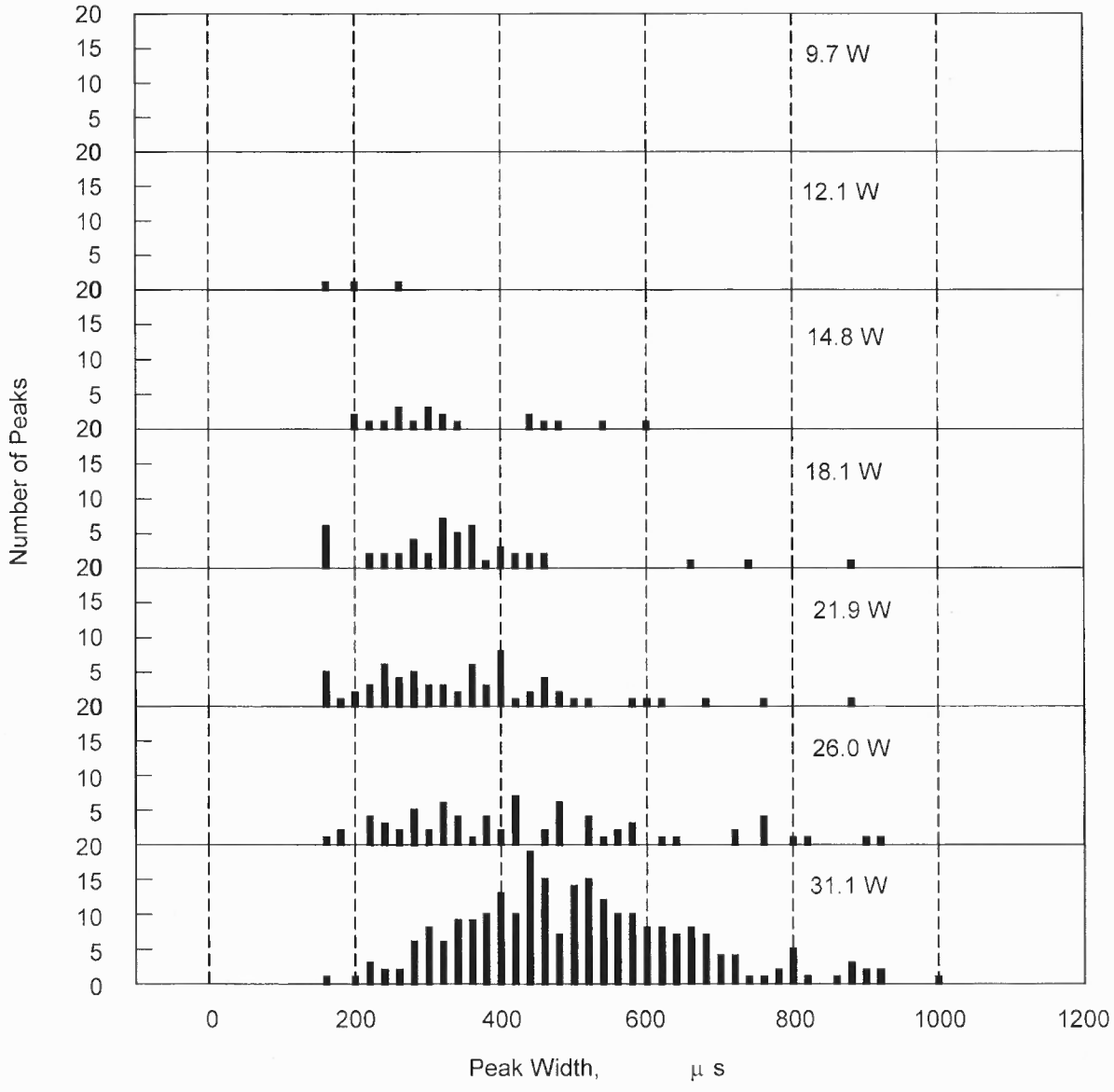

Figure 5.5 Frequency distribution of peak widths produced by emission of Al particles crossing the CO_2 laser beam in air. The aluminum aerosol jet speed is 1.5 m/s.

analysis is in agreement with peak width processing for detecting the laser power corresponding to the ignition threshold. It is also interesting to note that as the power increases, more and more particle combustion events are detected with the respective peak durations close to 900 μs. Because of the particle size-selective heating of Al particles in the CO_2 laser beam, it is reasonable to attribute this combustion duration to

the burn time of the particles most efficiently heated by the laser, i.e., the particles with the diameter of 3.4 μm. Using a burn time correlation proposed in Ref. [91] for combustion of aluminum aerosol, $t=310d$, the burn time of a 3.4 μm particle is 1054 μs. This is in good agreement with the measured time of 900 μs, which, in fact, is expected to be shorter than the predicted time because of a faster reaction expected for the particle while it is crossing the laser beam.

5.6 Results and Discussion

Experiments were conducted in five different environments shown in Table 5.1. The initial set of experiment was performed in air. The threshold laser power needed for ignition measured for air was slightly lower than shown in Chapter 4 which was attributed to focusing of the CO_2 laser beam at the calculated focal length for its wavelength of 10.6 μm. In earlier measurements focal length for the red laser (0.65 μm) was used to focus the CO_2 beam as well. The refocusing resulted in a tighter focal spot for the CO_2 laser beam. The new measurement in air was processed using a similar fitting procedure of matching the measured experimental laser threshold with that calculated as described in Chapter 4 and using the beam diameter as adjustable parameter. The fitting gave the beam diameter equal to 200 μm. This value was used as the beam diameter for processing all experiments in mixed environments, discussed in this chapter.

The experiments in air environments were repeated while turning on the heaters in the shroud jet hoses and in the elements of the aerosolizer. It was observed that pre-

heating the shroud gas to about 150 °C did not result in a meaningful difference in the measured laser power ignition thresholds.

Figure 5.6 shows the threshold laser power measured for all five different environments. For each environment, threshold power is measured for three different jet velocities, thus producing three different heating rates. An increase in the jet velocity increases the threshold power. CO_2/O_2 environment has the lowest threshold and H_2O/N_2 environment has the highest. Threshold for air is slightly higher than that for CO_2 O_2 which is due to higher amount of oxidizer. However, threshold for pure CO_2 environment is higher than that for air indicating O_2 to be a better oxidizer than CO_2. In mixed $H_2O/O_2/N_2$ environments, the ignition threshold depends strongly on the presence of O_2. Adding 14 percent by volume of O_2 to the environment with 35 percent of H_2O lowered the ignition threshold to effectively the same as for pure CO_2.

It was further considered whether a simplified Arrhenius ignition model approach could be useful for describing the ignition threshold results shown in Figure 5.6. The heat balance of a single particle as described in Chapter 4 is used here (*eqn. 4.1*).

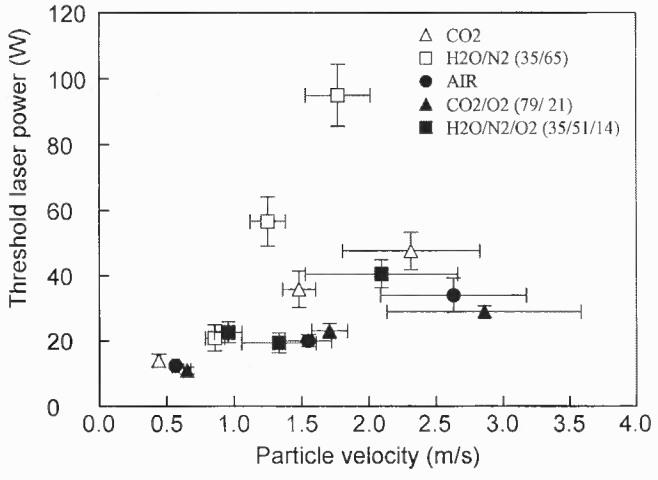

Figure 5.6 Threshold laser power required for ignition of aluminum particles crossing the laser beam in different gas environments (refer to Table 5.1 for environment details).

$$MC\frac{\partial T_p}{\partial t} = \dot{Q}_{Laser} + \dot{Q}_{Chemical} - \dot{Q}_{Radiation} - \dot{Q}_{Convection} \tag{5.1}$$

where M is the particle mass, C is its specific heat, T_p is its temperature; $\dot{Q}_{Laser}$ is the heat transfer rate to the particle from the laser beam, $\dot{Q}_{Chemical}$ is the chemical heat generation rate, and $\dot{Q}_{Radiation}$ and $\dot{Q}_{Convection}$ are the radiation and convection heat transfer rates, respectively. Convection term is given by the Fuchs model described in Chapter 3. $\dot{Q}_{Laser}$ and $\dot{Q}_{Radiation}$ are described in detail in Chapter 4. For a simplified approach, the chemical term is described by a single term Arrhenius ignition model,

$$\dot{Q}_{Chemical} = A_r \Delta H_{ox} P_{ox} (\pi d^2) \exp\left[\frac{-E_a}{RT_p}\right] \tag{5.2}$$

where A_r is the Arrhenius pre-exponent, ΔH_{ox} is the oxidation enthalpy (per mol of fuel), d particle diameter, P_{ox} oxidizer partial pressure, E_a activation energy and T_p particle temperature. For a given environment i.e. specific values of A_r, ΔH_{ox} and E_a, Equations 5.1 and 5.2 can be used to calculate temperature history of a particle of given diameter d. Note that for environments with several oxidizers, it is expected that the chemical term can be treated as a sum of the respective terms given by Eq. 5.2 taken for individual oxidizer species. Taking into account the selective heating of particles of around 3.4 μm by a CO_2 laser, these particles were expected to ignite first at the measured threshold laser power. Thus, equations 5.1 and 5.2 were used to calculate threshold laser power to best fit the experimental results in Figure 5.6 using A_r and E_a as variable parameters for each environment. The oxidation enthalpy, ΔH_{ox}, for each environment was calculated assuming oxidation of Al to Al_2O_3, given by equations:

$$Al(s) + O_2(g) \rightarrow Al_2O_3(s); \qquad \Delta H_{ox} = 1675.7\ kJ/mol \tag{5.3}$$

$$Al(s) + CO_2(g) \rightarrow Al_2O_3(s) + C(s); \qquad \Delta H_{ox} = 1282.1\ kJ/mol \tag{5.4}$$

$$Al(s) + 3H_2O(l) \rightarrow Al_2O_3(s) + 3H_2(g); \qquad \Delta H_{ox} = 950.1\ kJ/mol \tag{5.5}$$

When applied to different environments, this simple approach was capable of describing the ignition threshold measurements for air and CO_2/O_2. However, this approach was found to be problematic for other environments used in this study. It was observed that the heat transfer model presented above predicted that particles (d = 3.4 μm) will be heated to the temperature exceeding aluminum boiling point at the laser powers well below the measured ignition threshold, even if no chemical heat generation was included in the calculation, i.e., $\dot{Q}_{Chemical} = 0$. The results of this analysis are illustrated in Figure 5.7. Experimental points are shown for each environment separately. For each environment, the dashed lines show the calculated laser powers required to achieve 2792 K (the aluminum boiling point) with no chemical reaction allowed. Reaching the boiling of aluminum is considered to be an indicator of beginning of the vapor-phase combustion; in other words if the particle temperature reaches 2792 K, it is assumed that further analysis of heterogeneous reaction leading to ignition becomes irrelevant. Note that mismatch between the experimental and calculated trends is increasing for higher particle velocities. Further analysis of the calculation results shows that the slopes of the calculated (shown in Figure 5.7 as dashed lines) 'laser threshold power vs particle velocity' curves are strongly dependent on the size of the particles considered in the calculation. Figure 5.8 shows calculated threshold power curves for inert heating in H_2O/N_2 environment for different particle sizes. The slopes of the calculated curves become close to that of the experimental trend for 13 μm particle size. Adding a non-zero

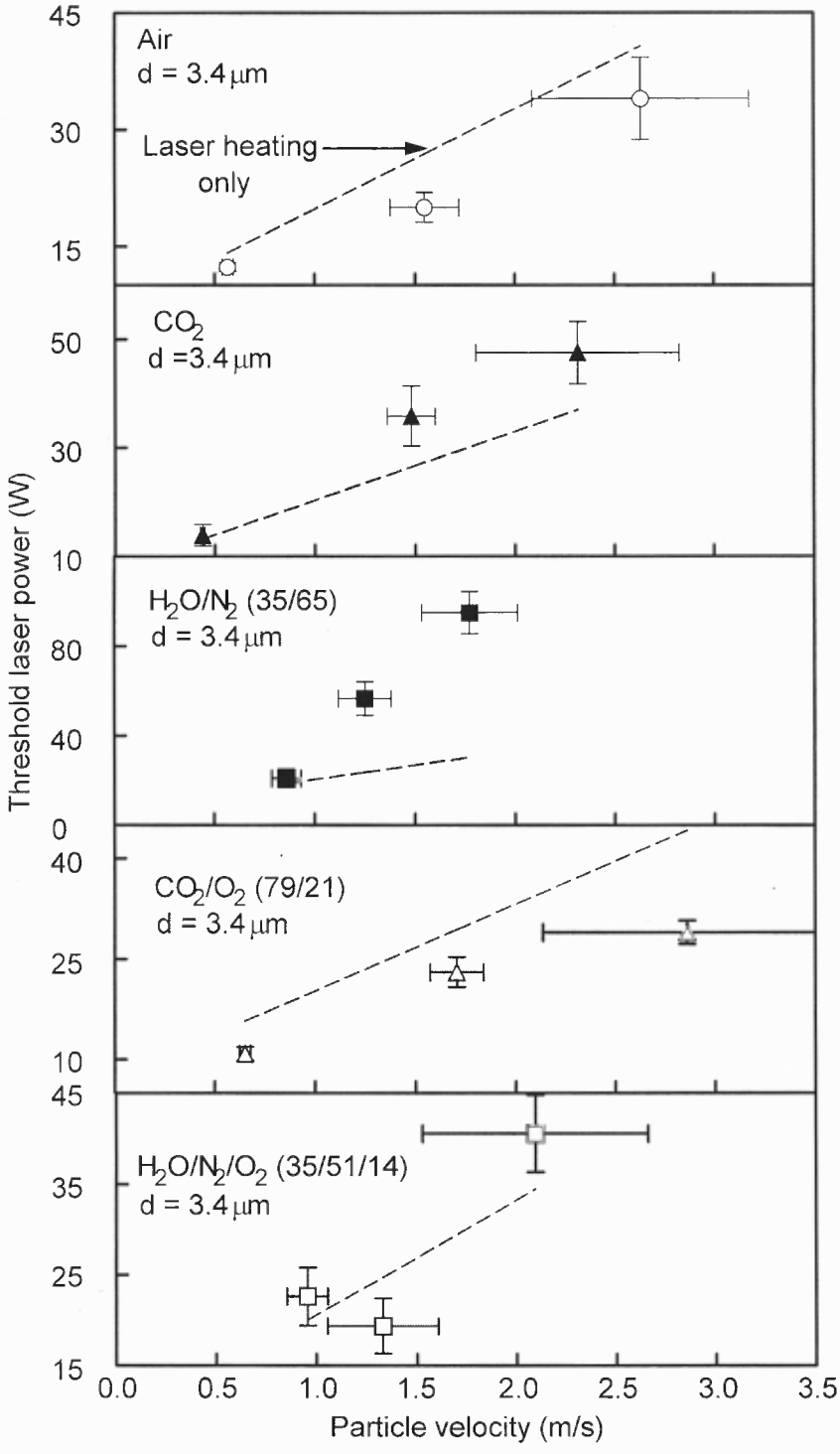

Figure 5.7 Heat transfer analysis describing laser heating for different environments for 3.4 μm Al particles compared to experimental laser power threshold required to observe ignition. Dashed lines show the laser powers required to achieve Al boiling point (2792 K) with no chemical reaction allowed.

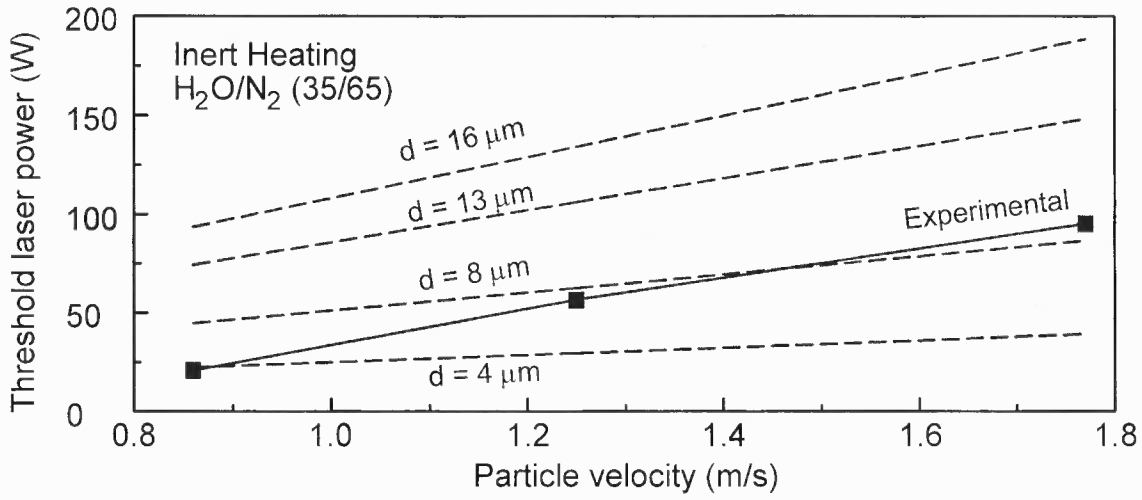

Figure 5.8 Slope of threshold power Vs Particle velocity is proportional to particle size. Calculation shows threshold power for inert heating in H_2O/N_2 environment for different particle sizes.

chemical term in the calculations affects the slope of the predicted trend only slightly.The primary effect is shifting the entire curve down. Thus, it can also be predicted that particles around 13 μm ignite at the threshold laser power. This analysis suggests that the assumption of only 3.4 μm particles igniting at the threshold power holds true for air and air / CO_2 environments only. It appears that for other environments, for which predicted threshold power for inert heating is higher than the experimental ignition thresholds, particles of size larger than 3.4 μm were observed to ignite instead.

The analysis presented below shows that this situation is indeed possible despite the fact that particles with diameter of 3.4 μm are the most efficient absorbers of the CO_2 laser energy. To understand this effect of environment, a simplified vapor phase droplet diffusion combustion model is analyzed for metal droplet combustion. This model is similar to the conventional particle combustion model; however the convective heat transfer is calculated using the transition regime heat transfer model appropriate for micron sized particles, for which Knudsen number $0.01<kn<0.1$.

5.6.1 Vapor Phase Combustion Droplet Model

To determine whether metal particles can achieve a vapor phase combustion regime, a simplified steady state aluminum droplet vapor phase combustion model is formulated. The model can predict if a vapor phase combustion is sustainable for a given particle size and oxidizer environment considering single particle burning in a room temperature gas. A spherical Al droplet at the aluminum boiling point (T_P = 2792 K) is assumed to be surrounded by a spherical flame with the flame temperature $T_F > T_P$. The model is intended to simulate the most favorable conditions for the vapor phase flame, so that when it is predicted that the flame is not sustainable, this result can be treated as conservative. To maximize the heat transfer from the flame to the particle surface and to minimize heat losses to the room temperature environment (both to simulate most favorable situation for vapor phase flame), the flame is assumed to be located right on the droplet surface. The heat balance for the flame is estimated assuming convective heat transfer to the particle, $\dot{Q}_P$, and losses to the surrounding environment, $\dot{Q}_E$, as shown schematically in Fgure 5.9. The heat input to the flame is from oxidation of the evaporated aluminum, $\dot{Q}_C$. For a sustainable combustion of the metal droplet the following inequality should be fulfilled:

$$\dot{Q}_C \geq \dot{Q}_E + \dot{Q}_P \tag{5.6}$$

The heat loss terms are calculated using Fuchs model described in Chapter 3 and can be written as:

$$\dot{Q}_P = f(T_P, T_F, d) \tag{5.7}$$

$$\dot{Q}_E = f(T_F, T_E, d) \tag{5.8}$$

where T_F is flame temperature, T_E is environment temperature and d is droplet diameter. The heat input to the flame is a function of the rate of droplet evaporation, which itself depends on the heat transferred from the flame to the droplet. Thus, $\dot{Q}_C$ can be calculated as:

$$\dot{Q}_C = \frac{\dot{Q}_P}{H_{eva}} \Delta H_{ox} \tag{5.9}$$

where, H_{eva} is the latent heat of evaporation for aluminum (so that the ratio of $\dot{Q}_P$ and H_{eva} gives the number of moles of Al evaporated per unit time) and ΔH_{ox} is the heat of oxidation of aluminum in the given environment. It is qualitatively clear that Equation 5.6 is easier to fulfill for higher flame temperatures, T_F and greater value of ΔH_{ox}. The flame temperature is not known and needs to be assumed for a simplified analysis.

Figure 5.9 To calculate heat transfer from flame to particle the particle is assumed to be surrounded by hot gas at the flame temperature T_F (left sketch). To calculate heat loss from flame to environment, the flame is assumed to sit directly on the particle surface and lose heat to the environment temperature T_E (right sketch).

As an example, Figure 5.10 shows the flame heat balance as a function of droplet diameter for assumed flame temperature of 3200 K and 2900 K. The solid lines indicate the total heat loss from the flame and the dashed line is the chemical heat released into the flame due to Al oxidation in air. For the flame temperature of 2900 K, the chemical

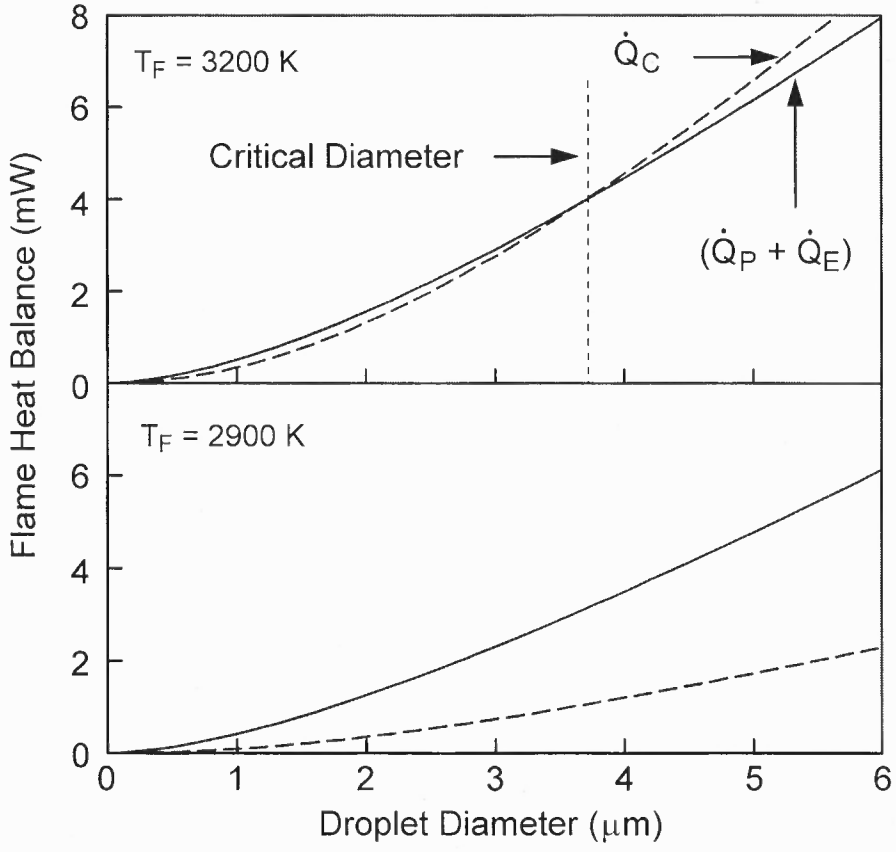

Figure 5.10 Flame heat balance as a function of droplet diameter for the flame temperatures of 3200 and 2900 K. The solid lines indicate total heat loss from the flame and the dashed lines show the chemical heat released into the flame due to Al oxidation in air.

heat input is always less than the flame heat loss so that vapor phase combustion is predicted to be impossible for any particle size. For the flame temperature of 3200 K, the chemical heat input exceeds the losses for the droplet size of more than about 3.7 μm. Thus, only the particles greater than 3.7 μm can burn in the vapor phase. This analysis indicates that it is impossible to fully combust Al particle of any size because during combustion, the droplet size will eventually reduce to below the critical droplet diameter. This analysis applies strictly to single particle combustion in a cold environment while in case of aerosols the flame heat loss to the environment is greatly reduced.

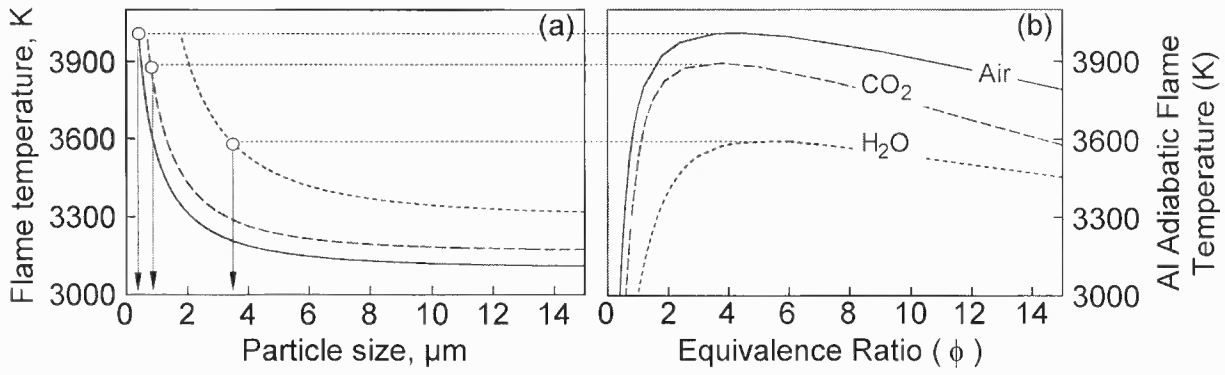

Figure 5.11 (a) Critical diameter plotted as a function of flame temperature for different environments; (b) adiabatic flame temperature of aluminum combustion plotted as a function of equivalence ratio for different environments. The critical diameter corresponding to the maximum flame temperature indicates the theoretical limit for vapor phase particle combustion for each environment.

The size dependence of combustion sustainability is the direct effect of Fuchs convection model which predicts lower Nusselt numbers for smaller particle. Thus for a given flame temperature, particles below certain critical size are not able to sustain vapor phase combustion. Note that, if flame heat losses were calculated using the continuum convection. the particle size dependence would not be observed. Instead, a minimum flame temperature needed to maintain vapor flame combustion would be predicted for all particle sizes.

Figure 5.11 (a) plots the minimum critical particle diameter against the assumed flame temperature for different oxidizer environments. It can be seen that higher flame temperatures are required to sustain combustion for smaller particle in H_2O and CO_2 environments as compared to that in air. This effect of environment is attributed to a higher oxidation enthalpy for aluminum in air, given by equations 5.3-5.5. The higher oxidation enthalpy helps supporting greater flame heat losses with smaller metal evaporation rates resulting in possibility of combustion for smaller particles. In addition,

higher oxidation enthalpy results in higher flame temperatures. For a conservative assumption, the flame temperature can be approximated by the adiabatic flame temperature for different environments. Figure 5.11 (b) shows adiabatic flame temperature for different environments as a function of equivalence ratio (equivalence ratio more than one indicates a fuel rich mixture). These temperatures were predicted using CEA code (CEA2, version 2, NASA Glenn) and considering constant pressure combustion case. The adiabatic flame temperature correlates with the oxidation enthalpy for different environments and peaks around equivalence ratio of 4. It should be noted that the actual flame temperature will always be less than the adiabatic flame temperature, and also the equivalence ratio existing in the flame is not a direct function of the oxidizer mole fraction in the environment; rather it is determined by diffusion of oxidizer and aluminum vapors to the flame. Horizontal lines connecting plots in Fig 5.11 (a) and 5.11 (b) show the critical particle sizes that can maintain the vapor phase flames in their respective environments assuming the highest possible flame temperature. Figure 5.11 shows that particle with size around 3.4 μm (the most efficient absorber of the CO_2 laser) and smaller are easily combustible in air which is why the model discussed above describes successfully the experimental results in Figure 5.7 for air and CO_2/O_2 environments. However, only much larger particles are predicted to be capable of maintaining vapor phase flame in pure H_2O and other environments. Note that the environments used in these experiments contained only 35% of H_2O with balance of N_2 resulting in a lower adiabatic flame temperature and thus a more severe restriction on the minimum particle size capable of achieving the vapor phase flame. Thus, the assumption of the fixed 3.4 μm particle size needs to be replaced and the sizes of particles ignited in

the CO_2 laser ignition experiments in water or other oxidizer environments need to be determined separately.

5.6.2 Arrhenius Model Parameter for Different Environments

Based on the above discussion, in spite of being the most efficient CO_2 laser absorber, the particle size of 3.4 μm may not always be the one observed to ignite at the threshold laser power. Rather, the size of the particle observed to ignite becomes a function of the environment. Thus, to extract Arrhenius model parameters for ignition kinetics i.e. A_r and E_a, the experimental trend for the threshold ignition power is fitted using Equation 5.1 and 5.2 considering A_r, E_a and d as adjustable parameters. Calculations were run to fit the experimental data for different gradually increasing particle diameters, activation energies and pre-exponents. Table 5.2 gives the best fit Arrhenius model parameters for different environments. For mixed environments, Arrhenius parameters from pure environments were used as per Equation 5.2 with contributions from different oxidizers added taking into account their respective values of the partial pressures.

Figure 5.12 shows the calculated best fit curves using the Arrhenius parameters (A_r and E_a) and particle diameter as adjustable parameters. The best fit parameters are tabulated in Table 5.2. The Arrhenius parameters are determined by processing results for single oxidizer environments. As noted above, the pure environment kinetics was used to process the results for dual oxidizer environments to determine the critical particle size igniting at ignition threshold laser power. Figure 5.12 shows that the match between the experimental and predicted laser ignition thresholds is equally good for pure oxidizers, for which Arrhenius kinetics was selected directly and for mixed environments, for which

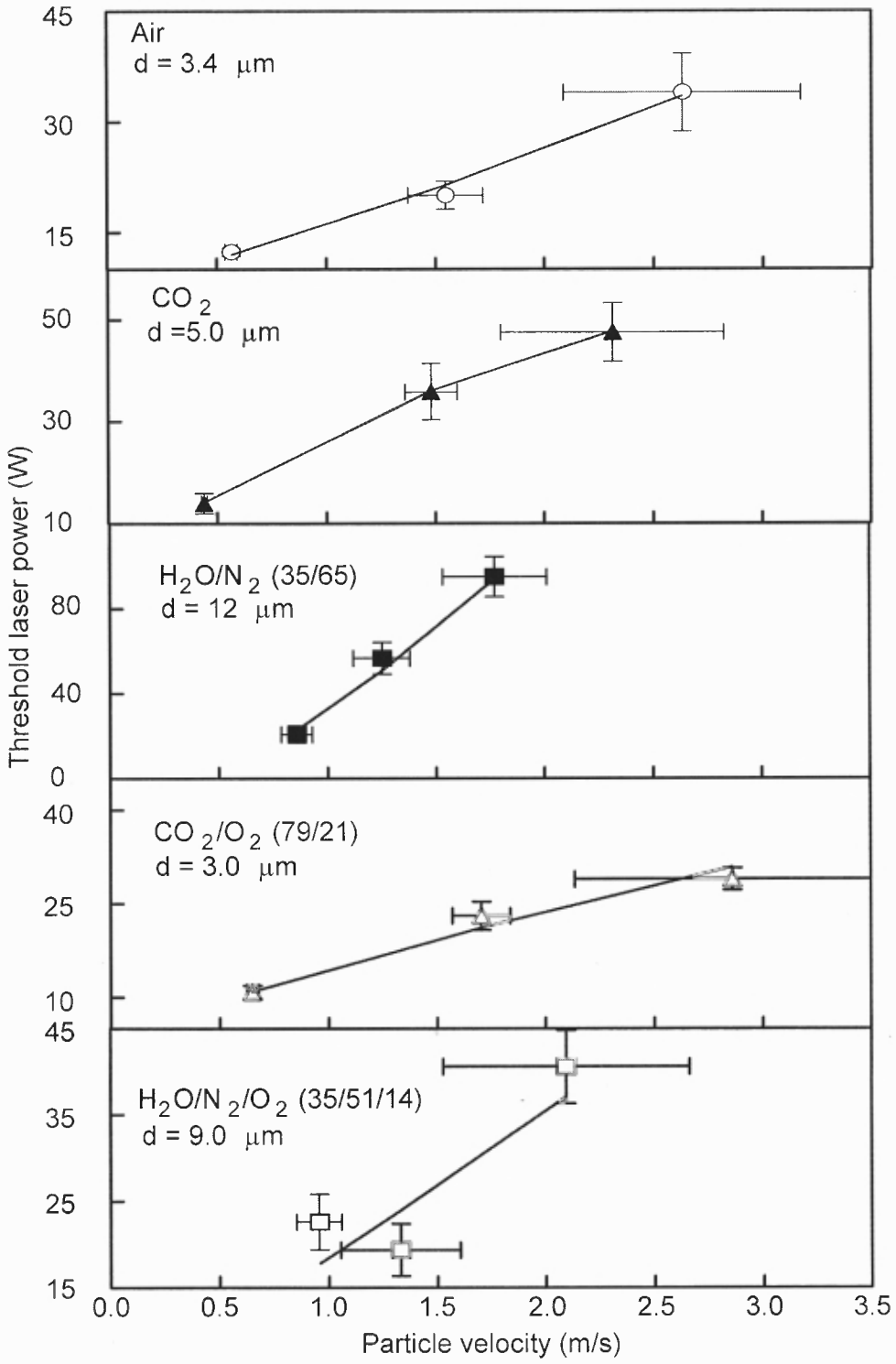

Figure 5.12 Best fit for experimental results fitted using a simplified Arrhenius model. Parameters extracted for pure environment tabulated in Table 5.2. Parameters for pure environments are added taking into account respective partial pressures to describe the mixed environments results.

Table 5.2 Arrhenius Parameters for Different Environments

Environments	*Air*	*CO_2*	*H_2O / N_2*	*H_2O / N_2 / O_2*	*CO_2 / O_2*
Volume (%)	(100)	(100)	(35/65)	(34/51/14)	(79/21)
Fitting Diameter (μm)	3.4	5.0	12.0	9.0	3.0
Z (s/m)	5.63E+03	3.94E+02	1.55E+10	---	---
Ea (kJ/mol)	179	154	192.5	---	---

the Arrhenius kinetics obtained for individual oxidizers was used considering respective particle pressures, according to Eq. (5.2).The processed results indicate that H_2O is associated with a faster ignition kinetics than O_2 and CO_2 environments. Note that it has lowest oxidation enthalpy.

It is concluded that in H_2O environment 12 μm sized particles ignite at the ignition threshold laser power. The O_2/H_2O environments has slightly smaller size particle of 9 μm burning at the threshold laser power which is reasonable considering that the flame temperature is expected to be higher when oxygen is added as an oxidizer. For other environments (O_2, CO_2 and mixed O_2/CO_2 oxidizers) the particle size is closer to the 3.4 μm.

The activation energy determined from the pure environment processing predicts the highest value for H_2O and lowest for CO_2. The pre-exponent, A_r for H_2O is very large as compared to those for O_2 and CO_2 environments, which are relatively close to each other.

5.7 Summary

Aluminum particle laser ignition experiments were conducted in five different oxidizer environments (Table 5.1). Three environments comprised of a single oxidizer i.e., O_2, CO_2 and H_2O and the other two were mixtures of two oxidizers i.e., H_2O/O_2 and CO_2/O_2. CO_2 laser ignition threshold power was measured for three different jet velocities for each environment. Experimental results for pure environments were processed and chemical kinetics (Arrhenius parameters, A_r and E_a) for Al ignition in respective environments were determined (Table 5.2). In spite of having higher measured threshold CO_2 laser power for ignition in the H_2O environment, the processed results predict faster kinetics for H_2O as compared to other oxidizers. Kinetics for O_2 and CO_2 environments are of similar order. The determined chemical kinetics for pure environments successfully described the experimental results for mixed environments.

The approach described in Chapter 4 for processing the experimental results by analyzing particle size of 3.4 μm only (because of the selective heating of this particle size) was modified. Based on the analysis of heat transfer for a simplified particle combustion configuration, it was established that there is a critical particle size below which the vapor phase combustion of individual metal particles is impossible. This conclusion is reached when transition heat transfer regime appropriate for micron-sized particles is considered, as opposed to the continuum convection approach suitable for particles with dimensions substantially greater than the mean free path of the molecule in the surrounding gas. Thus, when particles with diameters smaller than this critical dimension are heated by the CO_2 laser, self-sustained combustion in the vapor phase cannot be established even after the particle temperatures reach the metal boiling point.

This critical dimension depends on the oxidizing environment so that particles of different sizes were ignited at the measured threshold laser powers in different environments. Based on the processing of experimental data, it became possible to determine which particle size was igniting for which environment. The processing involved systematic analysis of the measured laser threshold energies taking into account different particle diameters and different values of Arrhenius parameters for the chemical heat release term. In environment with lower Al oxidation enthalpy, i.e., H_2O, larger particles were observed to ignite at the measured laser ignition threshold power.

CHAPTER 6

SUMMARY AND CONCLUSIONS

This work presents a new experimental technique and the corresponding heat transfer model that enables one to quantify ignition kinetics for reactive particles heated at varied heating rates approaching to or exceeding 10^6 K/s. Aluminum, the most common reactive metal additive is used in this study.

The experimental technique uses a focused CO_2 laser beam for heating micron-sized particles in an oxidizing environment. Because the laser's wavelength (10.6 μm) and particle diameters are comparable, the efficiency of the particle heating by the laser beam is highly dependent on particle sizes. At the threshold laser power, only particles with a very narrow range of sizes (around 3.4 μm) are heated efficiently and ignited. Thus, one needs to analyze the transient heat transfer only for the particles of this specific size, even though readily available poly-disperse powders are used in experiments. To ignite the particles, a laminar aerosol jet is fed into a focused CO_2 laser beam. The laser power is increased until the ignition is observed. A separate visible laser sheet is used to illuminate the particles in the jet for velocimetry. The particle speed could be readily controlled in the range of 0.1 - 3 m/s. The experiment is conducted in an oxidizing environment, so that if the laser power exceeds a specific threshold, the heated particles of 3.4 μm diameter start igniting when they cross the laser beam. The experiment involves measuring threshold laser ignition power and particle jet velocity. For any oxidizing environment experiments were repeated for three different jet velocities. This experimental data was processed to derive ignition kinetics of the environment.

A single particle heat transfer model to process the experimental measurements was developed. The developed heat transfer model includes radiation, convection in the transition regime, and a detailed analysis of the heat transfer from a laser beam to metal particles. A modified Fuchs transition regime heat transfer model was used to estimate convective heat loss from the particle to surrounding environment. Absorption of laser energy by the particle was calculated using Mie's scattering theory. The model considered heating rates on the order of 10^6 K/s achieved in the experiment, which are close to those occurring in many practical applications of metal-containing energetic materials. The model was calibrated comparing the calculations and experimental data acquired for spherical Al particles ignition in air, for which the ignition kinetics parameters were determined elsewhere. Calibration involved determining the diameter of the focal spot of the focused CO_2 laser beam. The developed experimental technique and the heat transfer model enabled us to quantify the kinetics of ignition of aluminum particle in a gaseous environment of interest.

The modified Fuchs' model for transition regime heat transfer was expanded to account for the properties of diatomic gases as a function of temperature. The dimensionless heat transfer coefficient, Nusselt number, was calculated as a function of particle diameter using this expanded Fuchs' model. Heat transfer rates predicted by the model are somewhat different from one another for the cases of particle heating and cooling while the absolute values of the particle-gas temperature difference are the same. This effect is not predicted by the continuum heat transfer calculations. It is observed that the applicability of the continuum heat transfer model for description of heating or cooling of particles of different sizes depends on pressure. For processes involving

particle heating by laser, particle ignition and similar processes, the continuum heat transfer model can be used for particles with diameters greater than about 10 μm at 1 bar, and for particles greater than about 1 μm at 10 bar pressure. Transition heat transfer model must always be used for analysis of heat transfer for nano-sized particles. For calculating ignition delay, the continuum model remains useful for particle diameters greater than, 18 μm and 2 μm for 1 and 10 bar, respectively. A usually poorly known accommodation coefficient is observed to have a relatively small effect on the heat transfer rate in the transition regime for metallic particles.

The developed CO_2 laser ignition technique was used to ignite aluminum particle in five different oxidizer environments. Three environments comprised of a single oxidizer i.e., O_2, CO_2 and H_2O and the other two were mixtures of two oxidizers i.e., H_2O/O_2 and CO_2/O_2. CO_2 laser ignition threshold power was measured for three different jet velocities for each environment.

The previous approach for processing the experimental results by analyzing particle size of 3.4 μm only (because of the selective heating of this particle size) was modified. Based on the analysis of heat transfer for a simplified particle combustion configuration, it was established that there is a critical particle size below which the vapor phase combustion of individual metal particles is impossible. This conclusion is reached when transition heat transfer regime appropriate for micron-sized particles is considered, as opposed to the continuum convection approach suitable for particles with dimensions substantially greater than the mean free path of the molecule in the surrounding gas. Thus, when particles with diameters smaller than this critical dimension are heated by the CO_2 laser, self-sustained combustion in the vapor phase cannot be

established even after the particle temperatures reach the metal boiling point. This critical dimension depends on the oxidizing environment so that particles of different sizes were ignited at the measured threshold laser powers in different environments. Based on the processing of experimental data, it became possible to determine which particle size was igniting for which environment. The processing involved systematic analysis of the measured laser threshold energies taking into account different particle diameters and different values of Arrhenius parameters for the chemical heat release term. In environment with lower Al oxidation enthalpy, i.e., H_2O, larger particles were observed to ignite at the laser ignition threshold power.

Experimental results for pure environments were processed and descriptive chemical kinetics (Arrhenius parameters, A_r and E_a) for Al ignition in respective environments were determined. In spite of having higher measured threshold CO_2 laser power for ignition in the H_2O environment, the processed results predict faster kinetics for H_2O as compared to other oxidizers. Kinetic parameters for O_2 and CO_2 environments are close to each other. The determined chemical kinetics for pure environments successfully described the experimental results for mixed environments

APPENDIX A

PMT SIGNAL PEAK WIDTH DISTRIBUTION FOR DIFFERENT OXIDIZING ENVIRONMENTS

Frequency distribution of PMT signal peak widths for different oxidizing environments is described in Section 5.5. Example of each environment is presented here. Each sub figure corresponds to a different CO_2 laser power used.

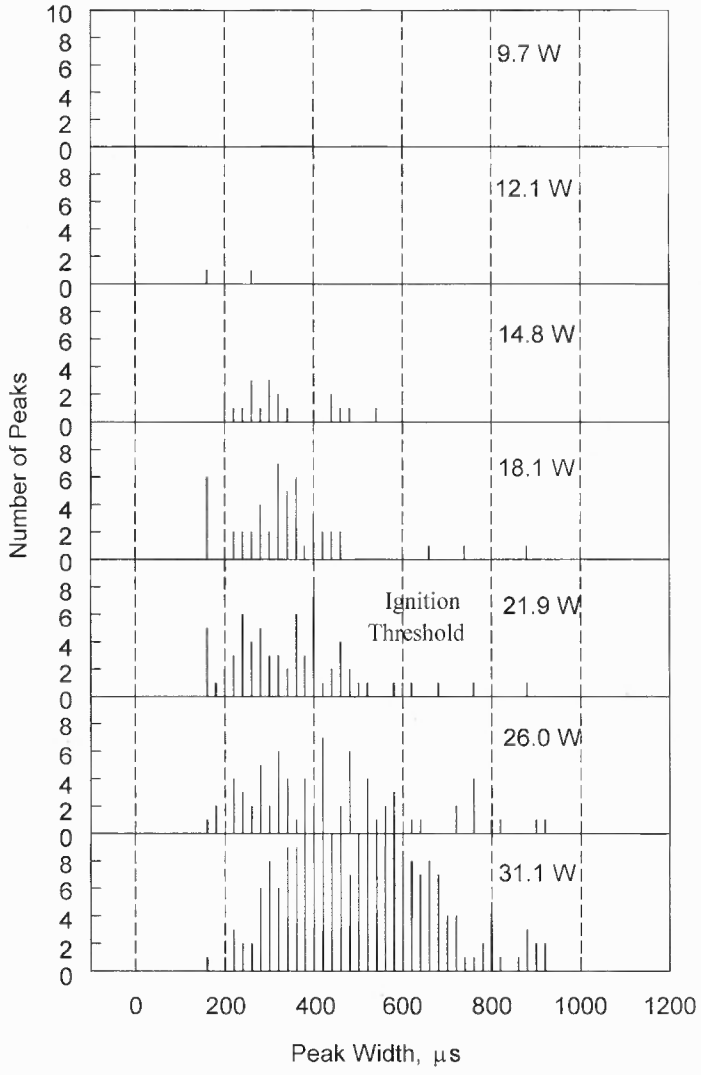

Figure A.1 Frequency distribution of peak widths produced by emission of Al particles crossing the CO_2 laser beam in air. The aluminum aerosol jet speed is 1.5 m/s.

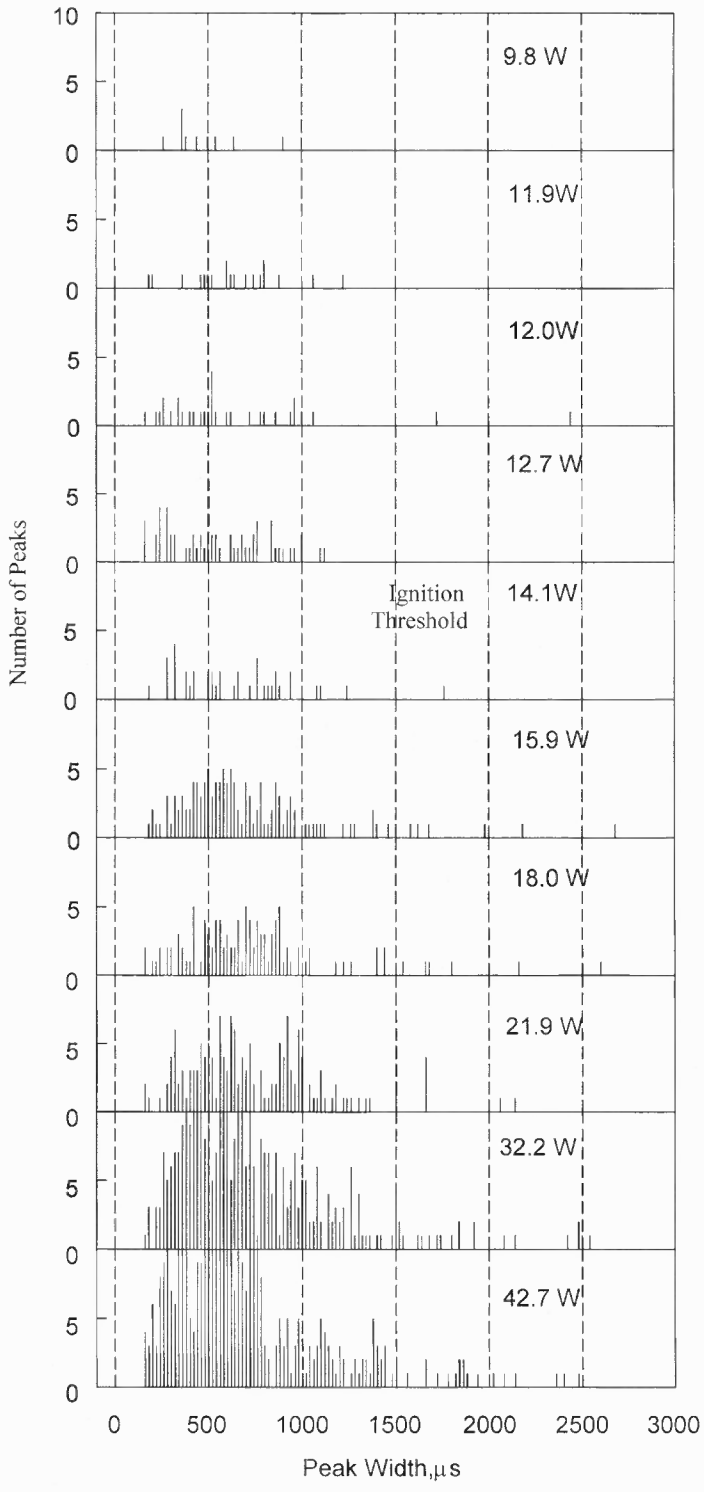

Figure A.2 Frequency distribution of peak widths produced by emission of Al particles crossing the CO_2 laser beam in CO_2. The aluminum aerosol jet speed is 0.4 m/s.

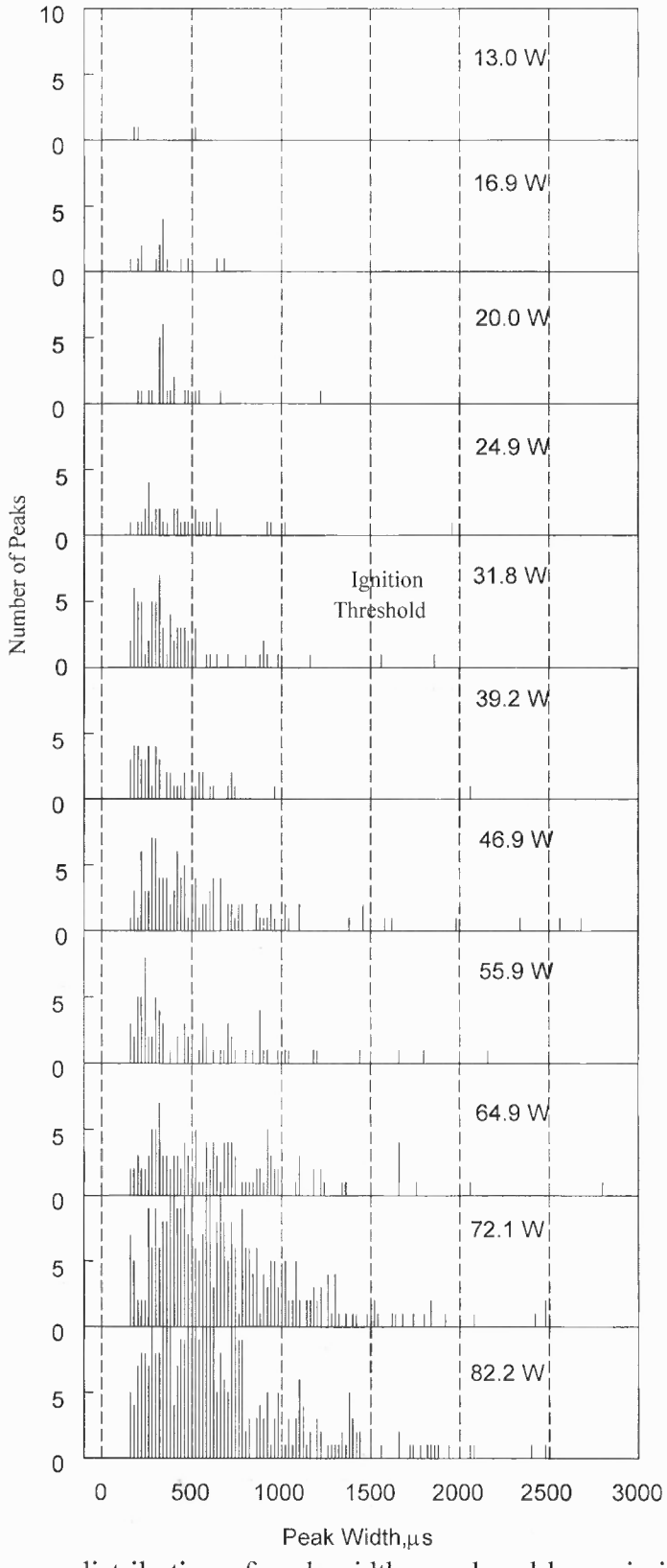

Figure A.3 Frequency distribution of peak widths produced by emission of Al particles crossing the CO_2 laser beam in H_2O. The aluminum aerosol jet speed is 0.86 m/s.

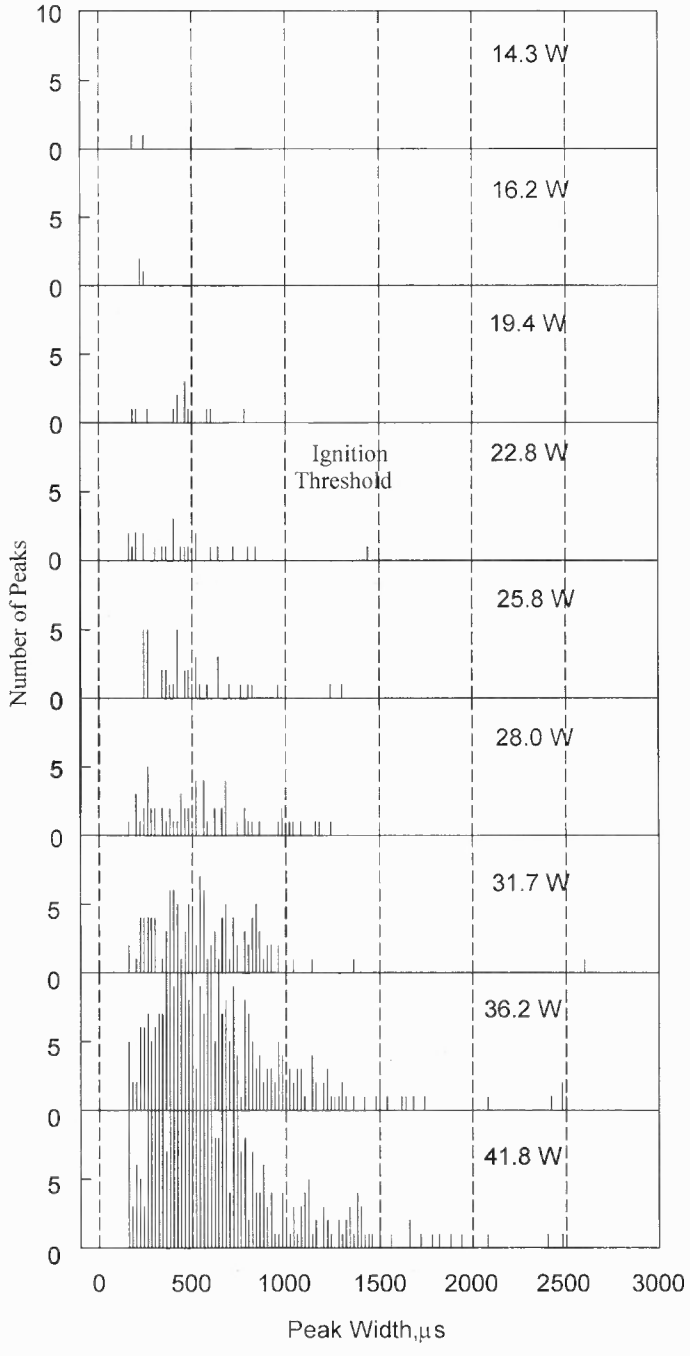

Figure A.4 Frequency distribution of peak widths produced by emission of Al particles crossing the CO_2 laser beam in H_2O/Air. The aluminum aerosol jet speed is 1.0 m/s.

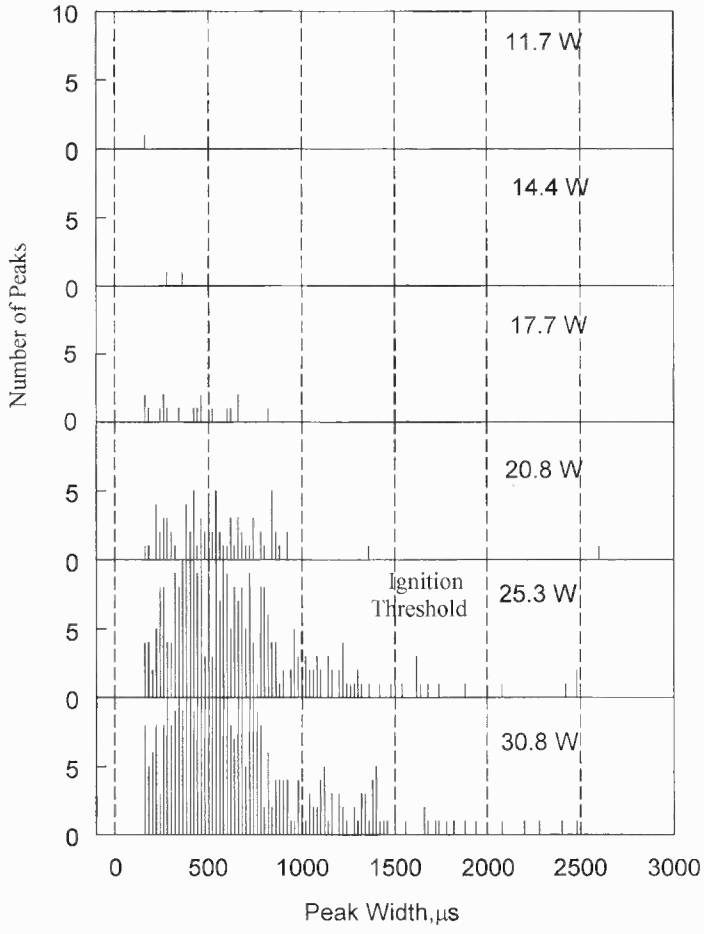

Figure A.5 Frequency distribution of peak widths produced by emission of Al particles crossing the CO_2 laser beam in CO_2/O_2. The aluminum aerosol jet speed is 1.7 m/s.

All the collected data is provided in files in the attached CD. The description of the CD files is listed in Appendix C. These results can be found in the mixed environment results folder.

APPENDIX B

FITTING PROCEDURE FOR DIFFERENT OXIDIZER ENVIRONMENTS

Fitting of the experimental results shown in Figure 5.12 is described here. Laser ignition threshold is calculated using Equation 5.1 with respective terms calculated as described in Chapter 5.

$$MC\frac{\partial T_p}{\partial t} = \dot{Q}_{Laser} + \dot{Q}_{Chemical} - \dot{Q}_{Radiation} - \dot{Q}_{Convection} \tag{B.1}$$

For any given environment, Equation B.1 has three unknowns i.e. particle diameter, d and two Arrhenius parameters, activation energy, E_a and pre-exponent Z. A 3D domain is defined by the three unknowns with activation energy varied between 120 KJ/mol and 350 KJ/mol by a step size of 0.5 KJ/mol. Pre-exponent; Z is varied between 10 and 10^{15} by a logarithmically increasing step size of $0.1\text{x}10^{\,n}$, where n=1, 2, 3...14. The particle diameter is varied by a step size of 1 μm from 2 to 20 μm. Laser ignition threshold is calculated for each point in this 3D domain. For each point the fit quality is calculated by R-squared value given by,

$$\begin{aligned} &R^2 = 1 - \frac{SSE}{SST} \\ &\textit{where} \\ &SSE = \sum\left(Y_j - \hat{Y}_j\right)^2 \\ &\textit{and} \\ &SST = \left(\sum Y_j^{\,2}\right) - \frac{\left(\sum Y_j\right)^2}{n} \end{aligned} \tag{B.2}$$

The variable point in 3D domain giving maximum R-squared value is the best fit solution. For example, to find best fit solution for any environment, laser ignition

threshold is calculated for the three different jet velocities (same as in experiments in this environment) for each possible combination of E_a and Z (varied according to the step size and range mentioned above), for a particle diameter d, say 2 μm to begin with. For each combination of E_a and Z, R-squared value is calculated using the experimental and calculated laser ignition threshold. This calculation sequence is repeated for all diameter in the range mentioned above with a step size of 1 μm. The combination of d, E_a and Z having maximum R-squared value is considered as the solution for Equation B.1. It should be noted that each experimental point represent one independent equation i.e. three independent equations are solved for three variables with this fitting procedure.

Table B.1 gives the solution of Equation B.1 for different environments. For mixed environments Arrhenius parameters calculated from pure environment (single oxidizer) results are used (as described by Equation 5.2). Thus, for mixed environments Equation B.1 is solved only for particle diameter, d

Table B.1 Solution of Equation B.1 for Different Environments

Environments	*Air*	CO_2	H_2O / N_2	H_2O / N_2 / O_2	CO_2 / O_2
Volume (%)	(100)	(100)	(35/65)	(34/51/14)	(79/21)
Fitting Diameter (μm)	3.4	5.0	12.0	9.0	3.0
Z (s/m)	5.63E+03	3.94E+02	1.55E+10	---	---
Ea (kJ/mol)	179	154	192.5	---	---
R^2	0.9972	0.9858	0.9998	0.7817	0.9583

APPENDIX C

DATA FILES

Experimental and calculation data files are provided in the attached CD. The list of the folders and description of the files contained is given below:

Folder	Description
01-Thesis Document	Complete thesis document as printed
02-Particle Heating by CO2 Laser	Matlab model files for Al single particle heating and ignition in air by CO_2 laser.
03-Transition Regime Heat Transfer	Matlab files for transition regime heat transfer model.
04-Al Ignition in Mixed Env	Matlab files for Al droplet combustion model, experimental data files and peak width data files.

REFERENCES

1. Evans, J.P., Borland, W., & Mardon, P.G. (1976). Pyrophoricity of Fine Metal Powders. Powder Metallurgy, 19 (1), 17-21.

2. Dugam, A.G., Muttalib, A., Gandhi, H.J., Phawade, P.A., John, A., & Khare, R.R.(1999). Effect of Fuel Content and Particle Size Distribution of Oxidizer on Ignition of Metal-based Pyrotechnic Compositions. Defence Science Journal, 49 (3), 263-268.

3. Rogers, R.N. (1975). Thermochemistry of Explosives. Thermochimica Acta, 11 (2), 131-139.

4. Pickard, J.M. (2002). Critical Ignition Temperature. Thermochimica Acta, 392-393, 37-40.

5. Annamalai, K., & Durbetaki, P. (1977). A Theory on Transition of Ignition Phase of Coal Particles. Combustion and Flame, 29 (2), 193-208.

6. Almada, S., Campos, J., & Gois, J. C. (1998). Ignition and Pyrolysis of Explosive Components. Proceedings of International Pyrotechnics Seminar, 24th, 827-831.

7. Ward, T.S., Trunov, M.A., Schoentiz, M., & Dreizin, E.L. (2006). Experimental Methodology and Heat Transfer Model for Identification of Ignition Kinetics of Powdered Fuels. International Journal of Heat and Mass Transfer, 49 (25-26), 4943-4954.

8. Shoshin, Y.L., Trunov, M.A., Zhu, X., Schoenitz, M., & Dreizin, E.L. (2006). Ignition of Aluminum-Rich Al–Ti Mechanical Alloys in Air. Combustion and Flame, 144 (4), 688–697.

9. Alekseev, A. G., Barlas, R. A., Tsidelko, T. I. & Shapoval, A. F. (1971). Effect of Particle Size on the Combustibility and Explosion Parameters of Dispersed Aluminum and Magnesium Powders. Editor: Nedin, V. V. In Preduprezhdenie Vnezapnykh Vzryvov Gazodispersnykh Sist, 66-73.

10. Assovskiy, I.G., Zhigalina, O.M. & Kolesnikov-Svinarev, V.I. (1999). Gravity Effect in Aluminum Droplet Ignition and Combustion. Fifth International Microgravvity Combustion Workshop, Clevelend, OH.

11. Belyaev A.F., Frolov, Yu. V. & Korotkov, A.I (1968). Combustion and Ignition of Particles of Finely Dispersed Aluminum, Fizika Goreniya i Vzryva, 4, 323-329.

12. Brossard, C., Ulas, A., Yen, C.L., & Kuo, K.K. (1997). Ignition and Combustion of Isolated Aluminum Particles in the Post-Flame Region of a Flat-Flame Burner, 16th International Colloquium on the Dynamic of Explosions and Reactive Systems, Krakow, Poland.

13. Derevyga, M.E., Stesik, L.N. & Fedorin, E.A. (1977). Study of the Ignition and Combustion of Aluminum and Zinc in Air. Fizika Goreniya i Vzyva, 13, 852-857.

14. Ermakov, V. A., Razdobreev, A. A., Skorik, A. I., Pozdeev, V. V. & Smolyakov, S. S. (1982). Temperature of Aluminum Particles at the Moments of Ignition and Combustion. Fizika Goreniya i Vzryva, 18, 141-143.

15. Friedman, R. & Macek, A. (1962). Ignition and Combustion of Aluminum Particles in Hot, Ambient Gases. Combustion and Flame, 6, 9-19.

16. Johnson C., Parr T., Hanson-Parr D., Hollins R., Fallis S. & Higa K. (2000). Combustion and Oxidation of Metal Nanoparticles and Composite Particles. Proceedings of 37-th JANNAF Combustion Subcommittee Meeting, 539-551.

17. Merzhanov, A.G., Grigorjev, Yu. M., Galchenko, & Yu, A. (1977). Aluminum Ignition. Combustion and Flame, 29, 1-14.

18. Yuasa, S., Zhu Y., & Sogo, S. (1997). Ignition and Combustion of Aluminum in Oxygen/Nitrogen Mixture Streams. Combustion and Flame, 108, 387-396.

19. Zhu, Y. & Yuasa, Y. (1998). Effect of Oxygen Concentration on Combustion of Aluminum in Oxygen/Nitrogen Mixture Streams, Combustion and Flame, 115 327-334.

20. Trunov M. A. & Dreizin E.L. (2003). Ignition of Metastable Metal Based High Energy Density Fuels, Ninth International Workshop on Combustion and Propulsion, Villa arigola,19032 Lerici, La Spezia.

21. Rufino, B., Boulc'h, F., Coulet, M.V., Lacroix, G. and Denoyel, R. (2007). Influence of particles size on thermal properties of aluminum powder. Acta Materialia, 55(8), 2815-2827.

22. Jones, D., E. G., Vachon, M. K., Queenie S. M.; Turcotte, R. and Fouchard, R. (2003). Thermal study of hexanitrohexaazaisowurtzitane (CL-20). Proceedings of the NATAS Annual Conference on Thermal Analysis and Applications, 31st, 050/1-050/10.

23. Bailey, A., Cartwright, M. and Frota, O. (1999). Thermal cook-off studies on explosives. Proceedings of the International Pyrotechnics Seminar, 26th, 29-36.

24. Trunov, M.A., Schoenitz, M., and Dreizin, E.L. (2005). Ignition of Aluminum Powders Under Different Experimental Conditions. Propellants Explosives and Pyrotechnics, 30 (1), 36-43.

25. Trunov, M.A., Schoenitz, M., Zhu, X., and Dreizin, E.L. (2005). Effect of Polymorphic Phase Transformations in Al2O3 Film on Oxidation Kinetics of Aluminum Powders. Combustion and Flame, 140 (4), 310-318.

26. Trunov, M.A., Umbrajkar, S.M., Schoenitz, M., Mang, J.T., and Dreizin, E.L (2006). Oxidation and Melting of Aluminum Nanopowders. Journal of Physical Chemistry B, 110 (26), 13094-13099.

27. Trunov, M.A., Schoenitz, M., and Dreizin, E.L. (2006). Effect of Polymorphic Phase Transformations in Alumina Layer on Ignition of Aluminum Particles. Combustion Theory and Modeling, 10 (4), 603-624.

28. Brzustowski, T. A.& Glassman, I. (1964).Vapor-Phase Diffusion Flames in the Combustion of Magnesium and Aluminum –Part II Experimental Observations in the Oxygen Atmospheres. Progress in Astronautics and Aeronautics, AIAA New-York, 117.

29. Kuehl, D. K. (1965). Ignition and Combustion of Aluminum and Beryllium, AIAA Journal, 3, 2239.

30. Merzhanov, A. G., Grigorjev, Y. M. & Galchenko, Y. A. (1977). Aluminum Ignition. Combustion and Flame, 29, 1.

31. Mohan, S, Trunov, M.A. and Dreizin, E.L. (Oct. 26-29, 2003). Characterization of Al Powder Ignition. Technical Fall Meeting, Eastern State Section of Combustion Institute, Pennsylvania State University, PA, USA

32. Davis, W. P., Baer A. D. & N. W. Ryan (1982). A Shock-tube Ignition Study of a Utah Coal. Combustion and Flame, 58(3), 201-215

33. Gauthier B.M., Davidson D.F. and Hanson, R.K. (2004). Shock Tube Determination of Ignition Delay Times in Full-blend and Surrogate Fuel Mixtures. Combustion and Flames, 139, 300-311.

34. Baek S. W., Sichel M. and C. W. Kauffman (1990). Asymptotic Analysis of the Shock Wave Ignition of Dust Particles. Combustion and Flame, 81(3-4), 219-228.

35. Servaites J., Krier H., Melcher J. C. and R. L. Burton (2001). Ignition and Combustion of Aluminum Particles in Shocked H2O/O2/Ar and CO2/O2/Ar Mixtures. Combustion and Flames, 125, 1040-1054.

36. Tim Bazyn, Herman Krier, Nick Glumac (2006). Combustion of Nanoaluminum at Elevated Pressure and Temperature Behind Reflected Shock Waves. Combustion and Flames, 145, 703-713.

37. Rozenband, V. I. & Vaganova, N. I. (1992). A Strength Model of Heterogeneous Ignition of Metal Particles, Combustion and Flame, 88, 113.

38. Yuasa, S., Zhu, Y. & Sogo, S. (1997). Ignition and Combustion of Aluminum in Oxygen/Nitrogen Mixture Streams, Effects of Oxygen Concentration on Combustion of Aluminum in Oxygen/Nitrogen Mixture Streams. Combust. Flame, 108, 387.

39. Rozenband, V. I. (2004). Thermo-Mechanical Aspects of the Heterogeneous Ignition of Metals, Combustion and Flame, 137, 366.

40. L. Rai, A., Lee, D., Park, K. and Zachariah, M. R. (2004). Importance of Phase Change of Aluminum in Oxidation of Aluminum Nanoparticles. J. Phys. Chem. B. (Letter), 108(39), 14793-14795.

41. Levitas V. I., Asay, B. W., Son, S. F & Pantoya, M. (2006). Melt Dispersion Mechanism for Fast Reaction of Nanothermites. Applied Physics Letters, 89, 071909.

42. Doherty, P. E. and Davis R. S. (1963) Direct Observation of the Oxidation of Aluminum Single –Cristal Surfaces. Journal of Appl. Phys., 34, 619-628.

43. Thomas, K. and Roberts, M. W. (1961). Direct Observation in the Electron Microscope of Oxide Layers of Aluminum. Journal of Appl. Phys., 32, 70-75.

44. Steinheil A. (1934). The Structure and Growth of thin Surface Films on Metals on Oxidation in Air. Ann. Phys., 19, 465-483.

45. Ramaswamy A. L., Kaste P. and Trevino S. F. (2004). A Micro-version of the Physio-Chemical Phenomena Occuring in Nano-Particles of Aluminum. Energetic Materials, 12, 1-24.

46. Levin I, and Brandon D. (1998). Metastable Alumina Polymorphs: Crystal Structures and Transitions Sequences. J. Am. Ceram. Soc., 81, 1995-2012.

47. Qiu, T. Q., Longtin, J. P., and Tien, C. L. (1995). Characteristics of Radiation Absorption in Metallic Particles. Journal of Heat Transfer, 117 (2), 340-345.

48. Shoshin, Y., and Dreizin, E. (2002). Production of Well-Controlled Laminar Aerosol Jets and Their Application for Studying Aerosol Combustion Processes. Aerosol Science and Technology, 36 (9), 953-962.

49. Shoshin, Y. L. and Dreizin, E. L. (2004). Laminar Lifted Flame Speed Measurements for Aerosols of Metals and Mechanical Alloys. AIAA Journal, 42 (7), 1416-1426

50. Yilbas, B.S. (1997). Laser Heating Process and Experimental Validation. International Journal of Heat and Mass Transfer, 40 (5), 1131-1143.

51. Bozhko, I. V., Glazkov, N. I., Troitskii, S. R and Falkovskii, N. I. (1980) Breakdown voltage of inert gases at temperature of 300 – 2000 K. Zhurnal Prikladnoi Mekhaniki I Tekhnicheskoi Fiziki 1, 20-27.

52. Mohan S., Trunov, M. A. & Dreizin, E. L. (2008). Heating and Ignition of Metal Particles in the Transition Heat Transfer Regime. Journal of Heat Transfer, 130 (10), 104505 – 104509.

53. Ni, T., Pinson, J. A., Gupta, S., and Santoro, R. J. (1995). Two-Dimensional Imaging of Soot Volume Fraction by the Use of Laser-Induced Incandescence. Applied Optics, 34, 7083- 7091.

54. Shaddix, C. R. and Smyth, K. C. (1996). Laser-Induced Incandescence Measurements of Soot Production in Steady and Flickering Methane, Propane, and Ethylene Diffusion Flames. Combustion and Flame, 107, 418-452.

55. Hofmann, M., Bessler, W. G., Schulz, C. and Jander, H. (2003). Laser-Induced Incandescence for Soot Diagnostics at High Pressures. Applied Optics, 42(12), 2052-2062.

56. Krishnan, S. and George, P. (1998). Solid Fuel Ramjet Combustor Design. Progress in Aerospace Sciences, 34(3-4), 219-256.

57. Galfetti, L., De Luca, L. T., Severini, F., Meda, L., Marra, G., Marchetti, M., Regi, M. and Bellucci, S. (2006). Nanoparticles for Solid Rocket Propulsion. Journal of Physics: Condensed Matter, 18 (33), S1991-S2005.

58. Fedorov, A. V. and Gosteev, Y. (1998). A Physical-Mathematical Investigation of Magnesium Particle Ignition. Archivum Combustionis, 16(3-4), 137-152.

59. Bocanegra, P. E., Chauveau, C. and Gökalp, I. (2007). Experimental Studies on the Burning of Coated and Uncoated Micro and Nano-Sized Aluminum Particles. Aerospace Science and Technology, 11(1), 33-38.

60. Mitsui, R. and Tanaka, T. (1973). Simple Models of Dust Explosion. Predicting Ignition Temperature and Minimum Explosive Limit in Terms of Particle Size. Industrial & Engineering Chemistry Process Design and Development, 12(3), 384-389.

61. Going, J. E. and Snoeys, J. (2002). Explosion Protection with Metal Dust Fuels. Process Safety Progress, 21(4), 305-312.

62. Dreizin, E. L. and Hoffmann, V. K. (2000). Experiments on Magnesium Aerosol Combustion in Microgravity. Combustion and Flame, 122(1-2), 20-29.

63. Legrand, B., Marion, M., Chauveau, C., Gökalp, I. and Shafirovich, E. (2001). Ignition and Combustion of Levitated Magnesium and Aluminum Particles in Carbon Dioxide. Combustion Science and Technology, 165(1), 151-174.

64. Cain, J. and Brewster, M.Q. (2006). Radiative Ignition of Fine Ammonium Perchlorate Composite Propellants. Propellants, Explosives, Pyrotechnics, 31(4), 278-284.

65. Liu, F., Daun, K. J., Snelling, D. R. and Smallwood, G. J. (2006). Heat Conduction from a Spherical Nano-Particle: Status of Modeling Heat Conduction in Laser-Induced Incandescence. Applied Physics B, 83, 355–382.

66. FIlipov, A. V. and Rosner, D. E. (2000). Energy Transfer between an Aerosol Particle and Gas at High Temperature Ratios in the Knudsen Transition Regime. International Journal of Heat and Mass Transfer, 43, 127-138.

67. McCoy, B.J. and Cha, C.Y. (1974). Transport Phenomena in the Rarefied Gas Transition Regime. Chemical Engineering Science, 29 (2), 381-388.

68. Kennard, E.H. (1938). Kinetic Theory of Gases, with an Introduction to Statistical Mechanics, McGraw-Hill, New York.

69. Williams, M.M.R. and. Loyalka, S.K (1991). Aerosol Science: Theory and Practice, Pergamon Press, New York.

70. Bhatnagar, P.L., Gross, E.P. and Krook, M. (1954). A Model for Collision Processes in Gases. I. Small Amplitude Processes in Charged and Neutral One-Component Systems. Physical Review., 94(3), 511 – 525.

71. Kullmer, R. (1996). Heat Transfer from Small Tungsten Spheres into an Ambient H2 Atmosphere. Applied Physics B, 62(2), 191-196.

72. Bird, G.A. (1994). Molecular Gas Dynamics and the Direct Simulation of Gas Flows, Clarendon Press, Oxford.

73. Fuchs, N.A. (1963). On the Stationary Charge Distribution on Aerosol Particles in a Bipolar Ionic Atmosphere. Geophys. Pura Appl. 56, 185-193.

74. Wright, P.G. (1960). On the Discontinuity Involved in Diffusion Across an Interface (the Δ of Fuchs). Discuss. Faraday Society, 30, 100-112.

75. Lees, L. (1965). Kinetic Theory Description of Rarefied Gas Flow. J. Soc. Ind. Appl. Math., 13, 278-311.

76. Lide, D. R. (2003-2004). Handbook of Chemistry and Physics, CRC, New York, US.

77. Roberts T.A., Burton and R.L. Krier, H. (1993). Ignition and combustion of aluminum/magnesium alloy particles in oxygen at high pressures. Combustion and Flame, 92 (1–2), 125–143.

78. Saxena, S. C., and Joshi, R. K. (1989). Thermal Accommodation and Adsorption Coefficients of Gases, Hemisphere Pub. Corp., New York, US.

79. Weast, R.C. (1977). CRC Handbook of Chemistry and Physics, 58th Edition, CRC Press, Cleveland OH.

80. Bhormen, C. F., and Huffman, D. R. (1983). Chap. 4 (126-129) in Absorption and Scattering of Light by Small Particles, Wiley, New York, US.

81. Graham, S. Arnold (1984). Absorptivity of Several Metals at 10.6 μm: Empirical Expressions for the Temperature Dependence Computed from Drude Theory. Applied Optics, 23 (9), 1434-1436.

82. Yilbas, B.S. (1997). Laser Heating Process and Experimental Validation. International Journal of Heat and Mass Transfer, 40 (5), 1131-1143.

83. Palik E.D. (1998). Handbook of Optical Constants of Solids III, Academic, New York.

84. Bazyn, T., Krier, H. and Glumac, N. (2007). Evidence for the transition from the diffusion-limit in aluminum particle combustion, Proceedings of the Combustion Institute 31 (II), 2021-2028.

85. Huang, Y., Risha, G.A.,Yang, V. and Yetter, R.A. (2007). Combustion of bimodal nano/micron-sized aluminum particle dust in air. Proceedings of the Combustion Institute, 31 (II), 2001-2009.

86. Dokhan, A., Price, E.W., Seitzman, J.M. and Sigman, R.K. (2002). The effects of bimodal aluminum with ultrafine aluminum on the burning rates of solid propellants. Proceedings of the Combustion Institute, 29 (2), 2939-2945.

87. DesJardin, P.E., Felske, J.D. and Carrara, M.D. (2005). Mechanistic model for aluminum particle ignition and combustion in air. Journal of Propulsion and Power, 21(3), 478-485.

88. Washburn, E.B., Trivedi, J.N., Catoire, L. and Beckstead, M.W. (2008) The simulation of the combustion of micrometer-sized aluminum particles with steam. Combustion Science and Technology, 180 (8), 1502-1517.

89. Price, E.W. (1984). Combustion of metalized propellants. Progress in Astronautics and Aeronautics, 90, 479-513.

90. Gilev, S.D. and Anisichkin, V.F. (2006). Interaction of aluminum with detonation products. Combustion, Explosion and Shock Waves, 42 (1), 107-115.

91. Shoshin, Y.L., and Dreizin, E.L. (2006) Particle combustion rates for mechanically alloyed Al–Ti and aluminum powders burning in air. Combustion and Flame 145 (4), 104505-105505.